NANOSTRUCTURED TITANIUM OXYNITRIDE-SUPPORTED IRIDIUM OXIDE OXYGEN EVOLUTION ELECTROCATALYST FOR WATER SPLITTING

by

Randall Archer, B.S.

A thesis submitted to the Graduate Council of
Texas State University in partial fulfillment
of the requirements for the degree of
Master of Science
with a Major in Chemistry
August 2018

Committee Members:

Christopher Rhodes, Chair

Benjamin Martin

Gary Beall

FAIR USE AND AUTHOR'S PERMISSION STATEMENT

Fair Use

Duplication Permission

ACKNOWLEDGEMENTS

The author would like to thank group members, Sibo Niu and Yuanfang Ying for their advice in thesis writing, and Dr. Fernando Godinez-Salomon for investing his time to teach about material synthesis and training on the rotating disc electrode. Thanks are due to Dr. Ben Martin for assisting with key equipment fabrication and to Dr. Christopher Rhodes for providing the opportunity to work on a challenging project. Thanks to all committee members who contributed their expertise and input to this work, Dr. Gary Beall, Dr. Ben Martin, and Dr. Christopher Rhodes.

TABLE OF CONTENTS

Page

ACKNOWLEDGEMENTS iv

LIST OF TABLES vii

LIST OF FIGURES viii

ABSTRACT v

CHAPTER

1. INTRODUCTION 1

    1.1 Overview of Hydrogen as a Renewable Fuel Source 1
    1.2 Background of Proton Exchange Membrane Water Electrolyzer (PEM-WE) 4
    1.3 Oxygen Evolution Reaction Principles and Electrocatalysts 6
    1.4 Prior Work on Supported OER Electrocatalyst 9
    1.5 Prior Work on Titanium Oxynitride as a Support for Electrocatalyst 13
    1.6 Specific Motivations for the Current Work 14

2. MATERIALS AND METHODS 15

    2.1 Chemicals 15
    2.2 Synthesis of Titanium Oxide Nanosheets 15
    2.3 Transformation of TiO_2 Nanosheets to Titanium Oxynitride 16
    2.4 Deposition of Iridium onto Titanium Oxynitride Support Material 16
    2.5 Physical, Structural, and Electrical Characterization 17
    2.6 Rotating Disk Electrochemical Characterization 18

3. RESULTS AND DISCUSSION 21

    3.1 Synthesis and Characterization of Titanium Oxynitride 21

3.1.1 Synthesis of TiO_xN_y 21
3.1.2 Characterization of TiO_xN_y 23
3.2 Synthesis and Characterization of Titanium Oxynitride Supported Iridium 30
3.2.1 Synthesis of Titanium Oxynitride Supported Iridium 30
3.2.2 Characterization of Titanium Oxynitride Supported Iridium 31
3.3 Electrochemical Characterization 34
3.3.1 Cyclic Voltammetry at Low Potential Range 34
3.3.2 Carbon Monoxide Stripping 36
3.3.3 Oxidation of Catalyst and Support by Cyclic Voltammetry 38
3.3.4 Oxygen Evolution Activity of Titanium Oxynitride Supported Iridium Oxide Electrocatalyst 42
3.3.5 Comparing Catalyst Activity and Stability 48
4. CONCLUSIONS 53

LITERATURE CITED 55

LIST OF TABLES

Table **Page**

1. Diffraction data for TiO_2-N800 and reference TiN (PDF01-087-0630). 28

2. Surface Area and Conductivity Measurements 30

3. Weight percent and atomic percent values for elemental mapping of TiO2-N800-Ir from electron dispersive spectroscopy featured in Figure 16. 33

4. Comparison of iridium oxide standard from Alpha Aesar with TiO_2-N800-Ir-EO mass and geometric activity normalizations before and after endurance testing..... 51

LIST OF FIGURES

Figure **Page**

1. Diagram showing existing green energy production methods (on left), hydrogen production (in center), and the many applications that could utilize hydrogen (on right).[1] 2

2. A) Sources of hydrogen production. B) Energy consumption for a variety of hydrogen sources. C) Table of global hydrogen consumption.[5] 3

3. Hybrid energy system featuring photovoltaics (PV array), solid oxide fuel cell (SOFC), electrolyzer, and batteries.[6] 4

4. Diagram of components of a PEM-WE device that uses electricity to split water molecules into hydrogen and oxygen gas.[8] 5

5. Department of Energy projections for hydrogen production and delivery.[9] 6

6. Proposed oxygen evolution reaction mechanisms.[10] 7

7. Depiction of catalyst material iridium oxide supported by antimony doped tin oxide.[22] 10

8. Unit cell of A) anatase and B) rutile titanium oxide. Blue spheres represent titanium while red spheres represent oxygen.[25] 11

9. Bar graph showing the mass normalization OER performance of mixed metal catalyst on TiO_2 anatase or rutile and unsupported.[34] 13

10. Hydrolysis and condensation reactions for the growth of TiO_2 21

11. A) Process for synthesis of titanium oxide nanosheets in microwave reactor 23

12. Scanning electron microscopy of A) TiO_2-As prep B) TiO_2-N600 and C) TiO_2-N800. 24

13. A) X-ray diffraction of as prepared TiO_2 and two heat treatments in ammonia gas, TiO_2-N600 and TiO_2-N800. 27

14. Crystal structure of cubic TiN.[48] 29

15. A) Synthesis of TiO_2-N800-Ir in microwave. 31

16. Electron dispersive spectroscopy of A) TiO2-N800-Ir with the following elements detected: B) oxygen C) titanium E) nitrogen and F) iridium. 32

17. X-ray diffraction of TiO_2-N800 and TiO_2-N800-Ir. 34

18. CV of support material, TiO_2-N800, showing the 2nd and 20th cycle at a rate of 100 mV sec^{-1} in 0.1 $HClO_4$. 35

19. Cyclic voltammetry, 20 cycles at a rate of 100 mV sec^{-1} in 0.1 M perchloric acid for TiO_2-N800-Ir. 36

20. Carbon monoxide stripping of TiO_2-N800-Ir at a rate of 20 mV sec^{-1} in 0.1 M perchloric acid and the dashed red line shows the integrated peak. 38

21. Cyclic voltammetry of the bare gold electrode in 0.1 $HClO_4$ taken at 100 mV s^{-1}. ... 39

22. Electrochemical oxidation of support material TiO_2-N800 in 0.1 $HClO_4$ taken at 100 mV s^{-1} for sixty cycles. 40

23. Electrochemical oxidation of A) TiO_2-N800-Ir for 60 cycles at a rate of 100 mV sec^{-1} in 0.1 M perchloric acid. 41

24. Initial chronoamperometry of TiO_2-N800-Ir-EO and standard IrO_2-AA. Values for IrO_2-AA provided by prior work.[59] 43

25. Tafel plots for TiO_2-N800-Ir-EO and IrO_2-AA derived from chronoamperometry measurement; potential range of 1.47-1.52 V..... 46

26. Bar graph showing the initial mass activity comparison of TiO_2-N800-Ir-EO and standard IrO_2-AA before accelerated endurance testing..... 47

27. Chronoamperometry of TiO_2-N800-Ir-EO and standard IrO_2-AA before and after endurance test..... 49

28. Tafel plots of TiO_2-N800-Ir-EO and standard IrO_2-AA before and after accelerated endurance testing. 50

29. Bar graph showing the mass activity comparison of TiO_2-N800-Ir-EO and standard IrO_2-AA before and after accelerated endurance testing..... 51

LIST OF ABBREVIATIONS

Abbreviation **Description**

PEM-WE……...…...…Proton exchange membrane water electrolysis

BET……..……Brunauer−Emmett−Teller

CO…….Carbon monoxide

CO_2…….…...Carbon dioxide

CA……Chronoamperometry

DOE…….……..Department of Energy

ECSA…….....Electrochemical Surface Area

EDS……...Electron dispersive spectroscopy

EG…….Ethylene glycol

LSV……Linear scan voltammetry

OER…….Oxygen evolution reaction

RDS……...…….Rate determining step

RHE……...……...Reversible hydrogen electrode

SEM……...Scanning electron microscopy

TiO_2……...Titanium oxide

TiO_xN_y……...Titanium oxynitride

PVP……..……..Polyvinylpyrrolidon

XPS……..X-ray photoelectron spectroscopy

ABSTRACT

Proton exchange membrane water electrolyzers (PEM-WE) have garnered much interest lately because of their ability to produce storable hydrogen from the simple inputs of water and electricity. Two half reactions drive the production of hydrogen and oxygen gas at the cathode and anode respectively. Electrocatalysts are needed to improve the efficiency of such devices, especially at the kinetically hindered anode. Iridium, a precious metal, has been the ideal catalyst for many years due to its excellent activity for the oxygen evolution reaction (OER) and reasonable stability in the harsh PEM-WE environment. The scarcity of this metal makes it prohibitively expensive for upscaled devices. Support materials have been studied to help reduce the cost of utilizing iridium-based catalysts. Traditionally, carbon has been used as support material in many other catalytic applications, but its stability is poor in a PEM-WE due to the low pH and high anodic potentials required to promote the OER. This study evaluates the use of a nanostructured titanium oxynitride (TiO_xN_y) as a support material for an iridium OER electrocatalyst. A three-step process was used to synthesize the material: (i) solvothermal synthesis of high surface area titanium oxide (TiO_2) nanosheets, (ii) heat and atmosphere treatments to transform TiO_2 into conductive TiO_xN_y, and (iii) deposition of iridium onto the TiO_xN_y support material. The initial OER mass activity of the titanium oxynitride-supported iridium catalyst (TiO_2-N800-Ir-EO) was measured to be six times larger than a standard iridium oxide material. The stability of TiO_2-N800-Ir-EO showed significant degradation after an accelerated endurance test. Support materials that provide enhanced

activity and improved stability with reduced precious metal loading will allow for the wider use of upscaled PEM-WE devices in electrical grid integration and automotive hydrogen fuel stations.

1. INTRODUCTION

1.1 Overview of Hydrogen as a Renewable Fuel Source

Non-renewable fossil fuels have dominated the energy market for over a hundred years. These fuels such as coal, refined oil, and natural gas all have an environmental impact due to the release of carbon dioxide (CO_2) gas upon their combustion. There are a variety of alternative energy sources now available including solar, wind, geothermal, and nuclear that have visions of becoming competitors to fossil fuels. Hydrogen, as an energy carrier, could be an important tool to help change how we convert, store, and consume energy. Electricity from renewable sources can provide the feedstock energy to generate hydrogen with an electrolyzer and then store it for later use in a variety of different applications (Figure 1).

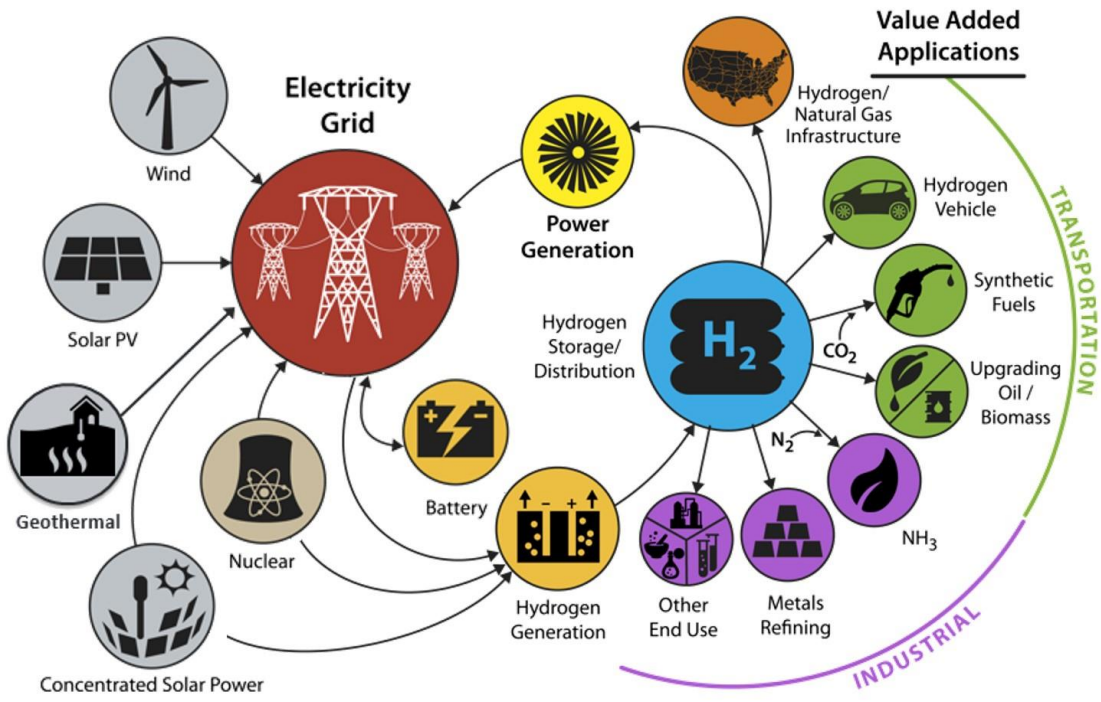

Figure 1. Diagram showing existing green energy production methods (on left), hydrogen production (in center), and the many applications that could utilize hydrogen (on right).[1]

Industrial uses for hydrogen include petrochemical refining, fertilizer production, metallurgical applications, and polysilicon growth in electronics.[2] The next wave of automotive innovation features hydrogen-powered vehicles which will surely help bolster the demand for electrolyzers.[3] The integration of solar/wind energy collection with hydrogen storage is being sought to improve the efficiency of large scale energy grids.[4] A published study in 2011 shows a general overview of the production and utilization of hydrogen en masse.[5] A simple pie chart shows that nearly all hydrogen is produced from CO_2 emitting, non-renewable resources (Figure 2A).

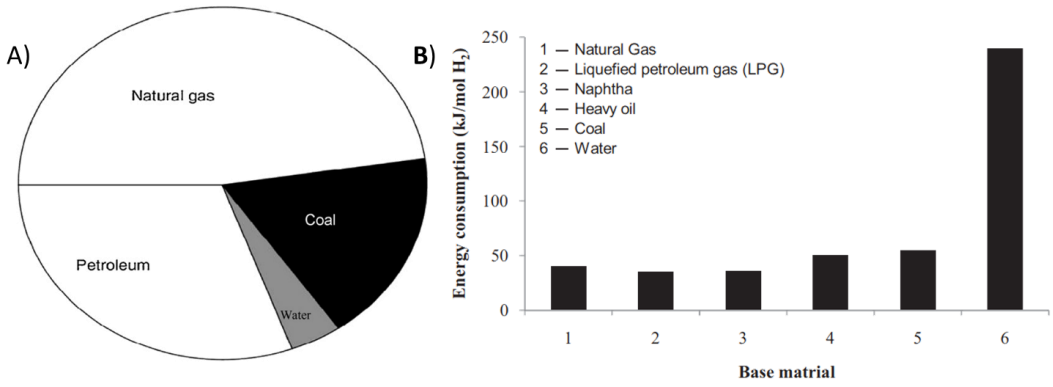

C)

Category	Hydrogen consumed	
	Billion m^3	Share (%)
Ammonia producers	273.7	61
Oil refineries	105.4	23
Methanol producers	40.5	9
Others	13.6	3
Merchant users	16.1	4
Total	449.3	100

Figure 2. A) Sources of hydrogen production. B) Energy consumption for a variety of hydrogen sources. C) Table of global hydrogen consumption.[5]

The energy input per mol of hydrogen gas is four to five times larger from water sourced hydrogen compared to other techniques (Figure 2B). The bulk of produced hydrogen is consumed in the synthesis of ammonia (61%) and the refinement of oil (23%) (Figure 1C). Improvements in water sourced hydrogen production and its implementation into energy solutions could change this landscape in the future. Water electrolyzers also can be implemented to combat the intermittent energy collection provided by renewable technologies such as wind and solar. Hassan et al. have reported the design of an ambitious hybridized system (Figure 3) that has combined photovoltaics, fuel cell, electrolyzer, and batteries to collectively work with the national electric grid.[6]

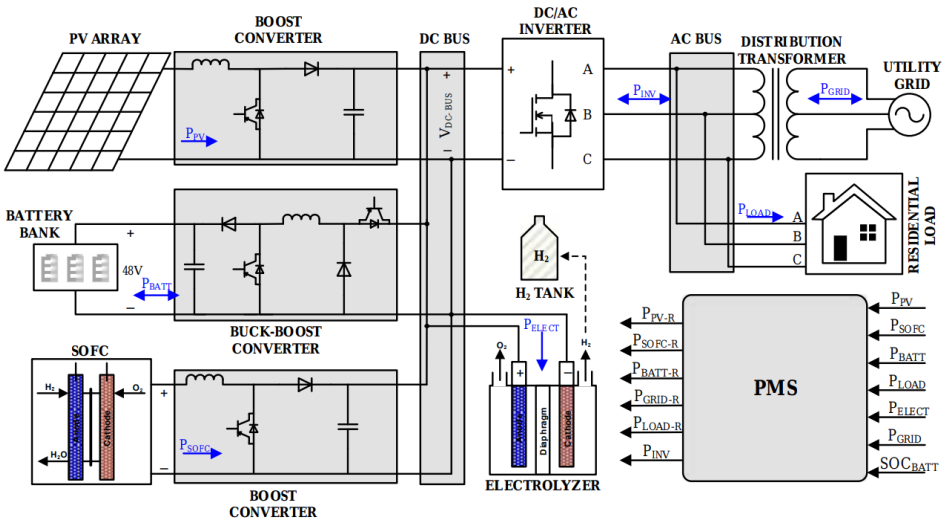

Figure 3. Hybrid energy system featuring photovoltaics (PV array), solid oxide fuel cell (SOFC), electrolyzer, and batteries.[6]

1.2 Background of Proton Exchange Membrane Water Electrolyzer (PEM-WE)

A proton exchange membrane water electrolyzer (PEM-WE) is an energy conversion device that can split water into hydrogen and oxygen gas. The PEM-WE is a two-electrode system with a polymer membrane serving as the electrolyte (Figure 4). The inputs for the device are electricity and water. At the anode, protons are electrolytically released from water to evolve oxygen gas in the first half reaction.

$$2H_2O \rightarrow O_2 + 4H^+ + 4e^- \quad E^0 = -1.23 \text{ V (RHE)} \qquad (1)$$

The protons then pass through the polymer membrane where they join with electrons to evolve hydrogen gas. The production of hydrogen in the second half reaction at the cathode is less kinetically hindered relative to the anode half reaction.[7]

$$4H^+ + 4e^- \rightarrow 2H_2 \qquad E^0 = 0.000 \text{ V (RHE)} \qquad (2)$$

The combined overall reaction shows the reaction products oxygen and hydrogen gas.

$2H_2O \rightarrow O_2 + 2H_2$ $E^0 = -1.23$ V (RHE) (3)

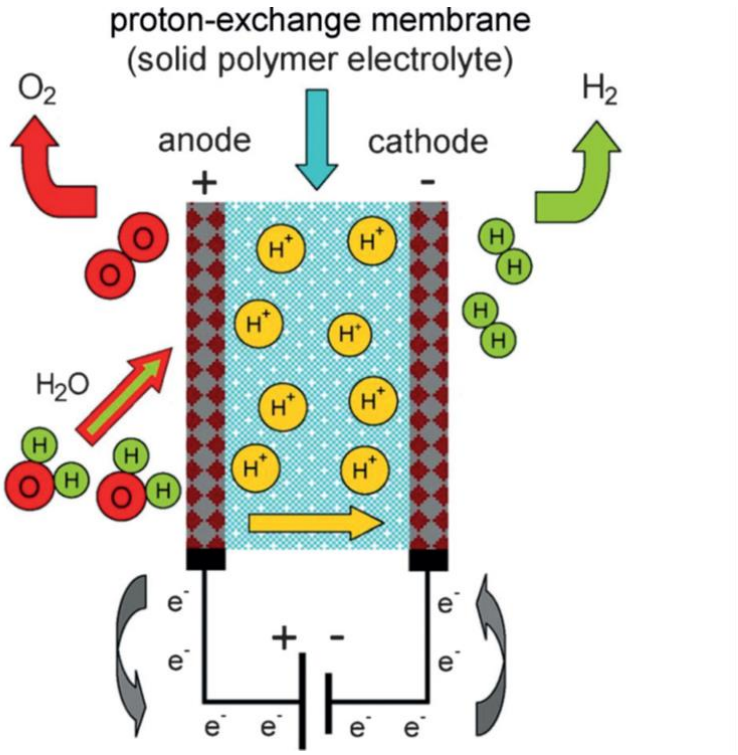

Figure 4. Diagram of components of a PEM-WE device that uses electricity to split water molecules into hydrogen and oxygen gas.[8]

The Department of Energy (DOE) has estimated projections for hydrogen production with respect to process, scale, and a three-tiered time frame (Figure 5). Established industrial processes should give way to renewably sourced technologies and water electrolysis will play a key role in both the mid-term and long-term solutions. The DOE's target cost for hydrogen production by an electrolyzer in 2015 was $3.90/kg and is expected to be lowered to $2.30/kg by 2020. There are many technical challenges to overcome in the scope of electrolyzers for these projections to deliver.

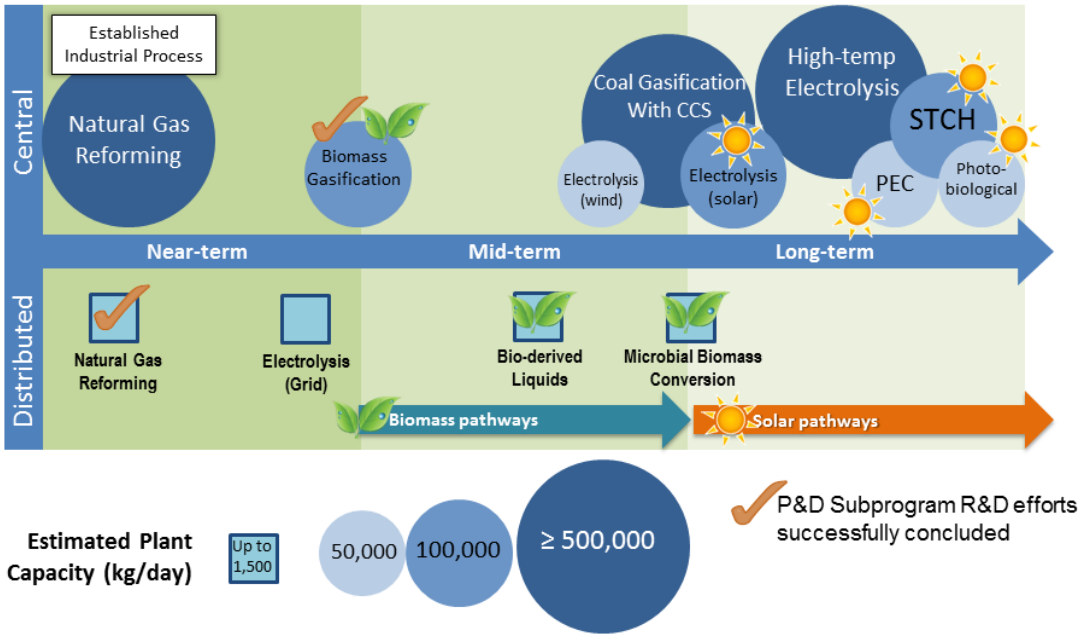

Figure 5. Department of Energy projections for hydrogen production and delivery.[9]

1.3 Oxygen Evolution Reaction Principles and Electrocatalysts

The oxygen evolution reaction (OER) occurs at the anode of PEM-WE device with the help of a catalyst material. The kinetic barriers of a reaction are largely defined by its mechanistic pathway. A mechanism can be thought of as a series of microtransactions involving differing intermediate chemical species in a larger process. The rate determining step (RDS) of a mechanism is the slowest chemical reaction that takes place. Prior work by Bockris asserts that the RDS in a mechanism can be determined by identifying the species of highest concentration on the catalyst surface.[7] Furthermore, Bockris concludes that the value of the Tafel slope (derivative of potential vs log current) from electrochemical measurements can be correlated with a particular RDS and its mechanism. There are four widely accepted mechanisms that have slightly differing RDS. Two oxide pathways and two peroxide pathways are shown in Figure 6.[10]

I)	Oxide Path	II)	Electrochemical Oxide Path
1)	$H_2O + M \rightarrow M\text{-}OH + H^+ + e^-$	1)	$H_2O + M \rightarrow M\text{-}OH + H^+ + e^-$
2)	$2\,M\text{-}OH \rightarrow M\text{-}O + M + H_2O$	2)	$M\text{-}OH \rightarrow M\text{-}O + H^+ + e^-$
3)	$2\,M\text{-}O \rightarrow 2\,M + O_2$	3)	$2\,M\text{-}O \rightarrow 2\,M + O_2$
III)	**Electrochemical Metal Peroxide Path**	**IV)**	**DFT-predicted Peroxide Path**
1)	$H_2O + M \rightarrow M\text{-}OH + H^+ + e^-$	1)	$H_2O + M \rightarrow M\text{-}OH + H^+ + e^-$
2)	$2\,M\text{-}OH \rightarrow M\text{-}O + M + H_2O$	2)	$M\text{-}OH \rightarrow M\text{-}O + H^+ + e^-$
3)	$M\text{-}O + H_2O \rightarrow M\text{-}OOH + H^+ + e^-$	3)	$M\text{-}O + H_2O \rightarrow M\text{-}OOH + H^+ + e^-$
4)	$2\,M\text{-}OOH \rightarrow M\text{-}O + H_2O + O_2 + M$	4)	$M\text{-}OOH \rightarrow M + O_2 + H^+ + e^-$

Figure 6. Proposed oxygen evolution reaction mechanisms.[10]

Water electrolysis is a non-spontaneous reaction that requires an input energy to drive it. The standard Gibbs free energy of a cell is equivalent to n, the number of moles, times F, Faraday's constant, times E^o, the standard potential of the cell.

$$\Delta G^o = -nFE^o \quad (4)$$

The change in Gibbs energy can also be related to a reaction constant K, the gas constant R, and standard temperature T. Combining both expressions for ΔG^o, the potential E^o of a cell can be solved for given a reaction constant K, as shown by the following equations.

$$\Delta G^o = RT \ln(K) \quad (5)$$

$$-nFE^o = RT \ln(K) \quad (6)$$

$$E^o = -(RT/nF) \ln (K) \quad (7)$$

The formation of water and its thermodynamic quantities also highlight some important fundamentals about the energy required for splitting water.

$$H_2(g) + O_2(g) \rightarrow H_2O(l) \quad (8)$$

$$\Delta G(-237\ kJ\ mol^{-1}) = \Delta H(-285\ kJ\ mol^{-1}) - T\Delta S(48\ kJ\ mol^{-1}),\ T=298K \quad (9)$$

$$E^{o}_{\Delta G}(-1.228\ V) = E^{o}_{\Delta H}(-1.481\ V) - E^{o}_{T\Delta S}(-0.253),\ T=298K \quad (10)$$

Equations 9 shows the Gibbs equation for water in units of kJ mol^{-1}. Using equation 4 the thermodynamic values can be converted into potential values. The Gibbs energy in equation 10 is equivalent to the equilibrium potential required to split water. The change in enthalpy is equivalent to the thermoneutral potential required to split water without the aid of heat and entropy from the term $T\Delta S$.

A kinetic barrier to OER requires that more energy must be applied to the system than the equilibrium potential, $E^0 = 1.23$ V.[11] This increased energy is called the overpotential, and when applied to an upscaled device, it equates to higher input cost.

Mass transport is an important factor in the overall efficiency of a working electrode for the OER. This movement of chemical species in solution and can be divided into three categories.[12] Diffusion is the movement of species with respect to a concentration gradient. Migration is movement of ionic species by an electric field. Convection is the simplest form of movement caused by general solution bulk movement. Most notably mass transport limitations for the OER occur when the product, oxygen gas, builds up on the working electrode. The oxygen gas blocks the reactant, water, from reaching the catalyst which results in halting of the reaction.

Many metals are unstable in acidic environments and especially so when high potentials are reached to promote the oxygen evolution reaction (OER) at the anode. Dissolution of even noble metals such as Pt, Ir, and Au at the anode has been observed during OER by Cherevko et al.[13] While highly active ruthenium and iridium can withstand the conditions better that other materials, their relative abundance is quite low,

which makes their use prohibitively expensive.[14] In addition to catalytic activity, the movement of reactants and products, or mass transport, is critical to the operation of the device. The design of the device must accommodate for the flow of water to the anode and removal of generated oxygen gas.[15]

The current state of the art anodes are made from ruthenium oxide or iridium oxide. Ruthenium can catalyze the reaction at a lower overpotential but is not as stable as iridium. The instability of a catalyst can be associated with its degree of dissolution. Reier et al. have shown that ruthenium dissolution is two to ten times higher when compared to iridium bulk and nanoparticle catatlyst.[16] Cherevko et al. report that amorphous iridium oxide is more stable than crystalline iridium oxide when tested in an acidic environment for the OER.[17] Catalyst materials in devices of scale will have to exhibit high stability at OER potentials while providing enhanced stability.

1.4 Prior Work on Supported OER Electrocatalyst

Precious metal catalysts have excellent activity and stability for the OER in acidic medium compared to other metals, but their rarity is a significant roadblock for investment into large scale applications. Support materials for these metals have been created with several criteria in mind: high surface area, conductivity, porosity, and durability. Precious metal loading has been reduced by coating or deposition onto a support material. The electronic conductivity of the support material must be sufficient (0.1 S cm^{-1}) to avoid ohmic drop potential to the active catalyst to promote catalysis.[10] Lower conductivities of support materials will lead to overall decreased performance of the electrocatalyst. The PEM-WE environment is acidic and OER potentials are typically

high (>1.5 V), so the support material must display high durability to resist corrosion. Porosity of the support material improves the electrochemical accessibility to the catalyst. Designer morphologies, such as Ni-Ir nanocages by Wang et al., have also improved catalytic activity as well as reduce precious metal loading.[18] Fine tuning of the electronic configuration of support materials by transition metal doping have also been attempted in many studies that include iron, antimony, and niobium.[19-21] Metal/metal-oxide support interaction have been probed by Oh et al. in a study with iridium oxide supported on antimony doped tin oxide (Figure 7).[22] In this work, core iridium metal was reported to be stabilized by the underlying support material and resulted in suppression of higher valency states for iridium in the oxide layer. Kumar and Ramani also report metal-support interactions for platinum on tantalum-modified titanium oxide electrocatalyst for the oxygen reduction reaction.[23]

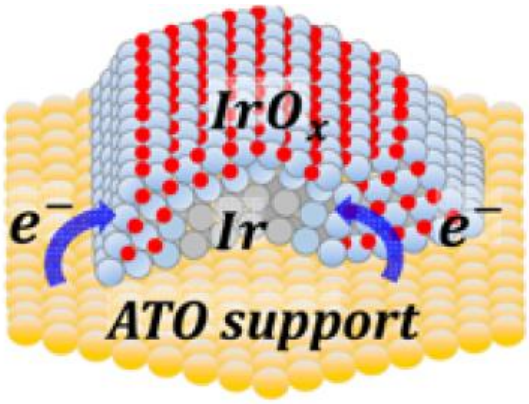

Figure 7. Depiction of catalyst material iridium oxide supported by antimony doped tin oxide.[22]

Titanium oxide (TiO_2) has been sought out as a support material because of its overall low toxicity, low cost, and high durability in acid.[24] Titanium oxide has two

dominiant polymorphs, anatase and rutile.[25] The unit cell for each can be seen in Figure 8. The particular polymorph that a material displays can be an important factor in how it reacts with its surroundings. Solar cells have been studied that had a high degree of a TiO_2 nanoparticle anatase 001 facets exposed.[26] This facet exposure control was found to improve efficiencies for solar cells.

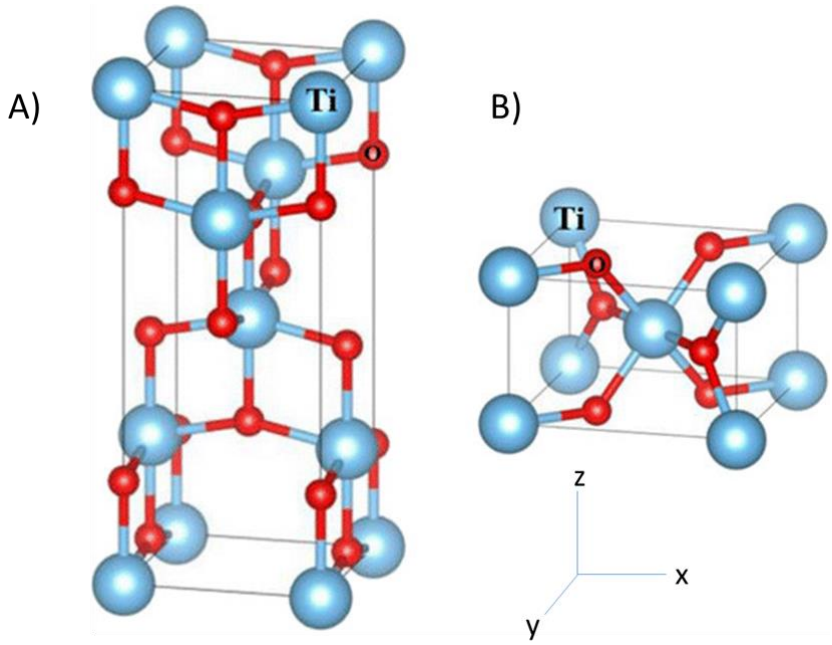

Figure 8. Unit cell of A) anatase and B) rutile titanium oxide. Blue spheres represent titanium while red spheres represent oxygen.[25]

Historically titanium and its oxides have been used widely as an anode for electrolysis of chlorine, chlorate and manganese dioxide.[27] TiO_2 has also proven to be versatile in its ability to be synthesized into many different morphologies including nanowires, nanosheets, and nanoparticles.[28-30] The conductivity of TiO_2 is quite low and can be classified as an insulator. Prior work by Hao et al. have improved its conductivy by doping it with niobium.[21] Another strategy employed by Mazur et al. was to create a

conductive matrix around TiO_2 with the active catalyst itself.[31] The study concludes that a balance must be met between the available surface area of the support material and the weight percent depostion of the active catalyst. TiO_2 has been explored as a support material for OER catalyst. Oakton et al. developed a single-step approach to synthesizing iridium oxide nanoparticles dispersed into rutile TiO_2 nanoparticles that showed improved activity and stability.[32] Moradi and Dehghanian have studied the effect of iridium oxide doping on TiO_2 supported ruthenium oxide anodes in acid.[33] Fuentes et al. have looked at mixed metal catalyst on TiO_2 support and found that Ir:Ru (1:1) on anatase TiO_2 (Figure 9) was similar to its rutile supported counterpart within experimental error but was higher than the unsupported mixed catalyst.[34] Titania has been utilized as a support for electrocatalysts, but its usefulness may be improved if its electronic conductivity could be raised significantly.

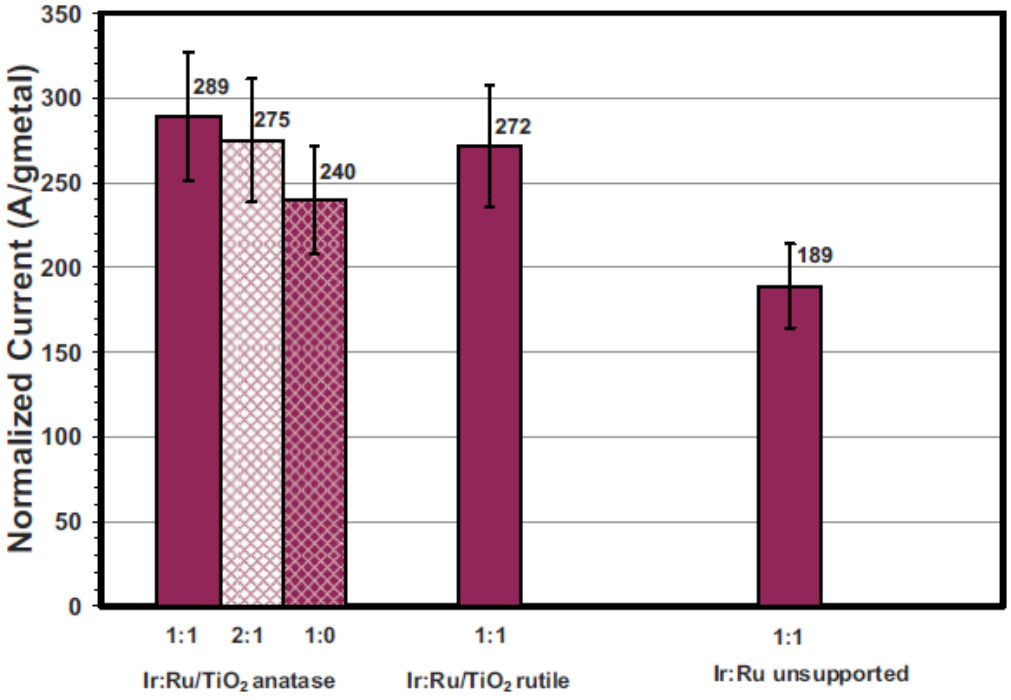

Figure 9. Bar graph showing the mass normalization OER performance of mixed metal catalyst on TiO_2 anatase or rutile and unsupported.[34]

1.5 Prior Work on Titanium Oxynitride as a Support for Electrocatalyst

Titanium oxynitride (TiO_xN_y) has been investigated as a support material for platinum catalyst for the oxygen reduction reaction because of its stability in acid and improved conductivity.[35-37] Gebauer et al. have examined synthetic conditions for titanium oxynitrides (TiO_xN_y) and evaluated its potential for OER.[38] Their study finds that nitridation of TiO_2 has a strong temperature dependence and is also affected by ammonia flow rates during heating. Low potentials (0-1.2 V_{RHE}) do not yield any oxidation or reduction evidence but an irreversible oxidation is apparent at high potential in the first cycle. Following electrochemical test, X-ray photoelectron spectroscopy

(XPS) indicates that surface oxidation converts TiN into TiO_xN_y and any present TiO_xN_y into TiO or TiO_2.

1.6 Specific Motivations for the Current Work

Improving activity and stability while maintaining low catalyst loadings are paramount for the advancement of OER catalysts. The objectives of this study are to i) synthesize and characterize titanium oxynitride (TiO_xN_y) by temperature and atmosphere treatments of TiO_2 nanosheets; ii) deposit iridium onto TiO_xN_y support material and characterize the material; iii) determine the electrochemical oxygen evolution activity and stability of a titanium oxynitride supported iridium oxide electrocatalyst. To the best of our knowledge, no one has reported an iridium electrocatalyst supported by titanium oxynitride for the OER.

2. MATERIALS AND METHODS

2.1 Chemicals

Titanium (III) chloride (20% w/v) solution in 2N HCl was purchased from Acros Organics. Ethylene glycol (reagent grade) and isopropanol (HPLC grade) were purchased from BDH. Ethylene glycol (99.5%) was purchased from TCI. Reagent grade ethylene glycol was used for synthesis and deposition of materials while 99.5% ethylene glycol was used for electrochemical ink solutions. Ultrapure water (18MΩ) was purchased form Ricca. Iridium (III) chloride hydrate ($IrCl_3 \cdot xH_2O$, 99.8%) was purchased from Alfa Aesar. The x variable was verified through the manufacturer to be 1.6 for this particular batch of precursor. Nafion perfluorinated resin (5 wt%, 15-20% water) and sodium hydroxide (97%) were purchased from Sigma-Aldrich. Perchloric acid (70%, double distilled) was purchased from Veritas GFC.

2.2 Synthesis of Titanium Oxide Nanosheets

To produce titanium oxide nanosheets, titanium (III) chloride (2 mL) was combined with ethylene glycol (reagent grade, 23 mL) and sodium hydroxide solution (2 mL, 1.26M) in a microwave reaction tube and allowed to spin under magnetic stirring for 5 minutes. The tube was placed in the microwave reactor (Discover SP) and was reacted at 150 ^{o}C for 13 minutes under microwave irradiation. The resulting precipitate was recovered by centrifugation (5000 RPM, 7 minutes). The initial spin was used to remove ethylene glycol and then the precipitate was rinsed with ultrapure water, typically in three subsequent steps of further centrifugation. A final rinse/centrifugation was done with HPLC grade isopropanol. The gathered precipitate was then dried overnight in a vacuum

oven at 50 ^{o}C. After drying the material was crushed with mortar and pestle into a fine powder.

2.3 Transformation of TiO_2 Nanosheets to Titanium Oxynitride

To transform the TiO_2 nanosheets into TiO_xN_y, 100 to 300 mg of the dried material was placed into a tube furnace and ammonia gas was flowed (~40 mL/min) for 10 minutes. The temperature was raised at 20 ^{o}C per minute until reaching 600 ^{o}C or 800 ^{o}C and then a dwell time of 2 hours was held. After the dwell time, the ammonia flow was maintained until the material returned to room temperature. Argon gas was then flowed for 20 minutes to purge ammonia. Sample names were then designated as TiO_2-NX (where X=600 or 800).

2.4 Deposition of Iridium onto Titanium Oxynitride Support Material

A support to catalyst weight percent (60/40 w/w) was then used to mix TiO_2-N800 and iridium (Ir) in ethylene glycol (reagent grade). Ir precursor ($IrCl_3 \cdot xH_2O$) was weighed and then sonicated in ethylene glycol for 10-15 minutes to reach full dissolution. The dissolved Ir precursor was added to TiO_2-N800 and a total of 25 mL of ethylene glycol in a microwave reaction tube and kept under magnetic stirring for 10-15 minutes. The mixture was then placed into the microwave reactor and reacted for 20 minutes at 120 ^{o}C. The resulting precipitate was centrifuged and dried in the same manner as the TiO_2.

2.5 Physical, Structural, and Electrical Characterization

A Bruker AXS D8 Advance powder X-ray diffractometer with a Cu Ka (λ = 1.5406 Å) radiation source, operating at 40 kV and 25 mA, with a high-resolution energy dispersive 1D Linxeye XE detector was used on powdered materials. An increment of 0.01° was applied over the range of $2.5° < 2\theta < 70°$. Powder diffraction references were used for comparison with measured materials; anatase TiO_2 (PDF 00-001-0562), rutile TiO_2 (PDF 00-001-1292), metallic iridium (PDF 00-006-0598), iridium oxide (PDF 01-088-0288), and titanium nitride (PDF 01-087-0630).

The morphology and elemental distribution of the catalysts was determined by scanning electron microscopy (SEM) using a FEI Helios Nanolab 400 DualBeam and coupled electron dispersive spectroscopy (EDS). Samples were dispersed into isopropanol and cast onto bare aluminum sample holder.

A Micromeritics ASAP 2020 surface area and porosimetry analyzer was used to collect Brunauer−Emmett−Teller (BET) surface areas by nitrogen physisorption. Samples were degassed under vacuum at 120 °C for 16 h prior to analysis.

Materials were placed in a HS Test Cell (Pred Materials International, Inc.) with a 10 kg force spring. The test cell was then connected to an Arbin BT2043 test station. A constant voltage (±5 mV) was applied to the cell in three-minute intervals in which the current reached a steady state. Electrical conductivity was then calculated using the following equations:

$$\sigma = l/RA \quad (11)$$

$$R = V/I \quad (12)$$

where voltage (V) is 5 mV, current (I) is the approximate steady state current, the material disc area (A) is 2.27 cm^2, and the length (l) is the measured thickness of the material disc.

2.6 Rotating Disk Electrochemical Characterization

Electrochemical measurements were performed on a rotating disk electrode (RDE) with an Autolab PGSTAT128N bipotentiostat (Pine Instruments) at constant temperature (298 K). A three-electrode cell configuration was used in 0.1 M $HClO_4$ electrolyte. The working electrode was made from a thin film casted from a synthesized catalyst unto a gold disc electrode (geometric area: 0.196 cm^2). A platinum mesh coil was used as the counter electrode and the reversible hydrogen reference electrode was prepared by bubbling hydrogen gas on a platinum wire. The cell was purged with argon for ten minutes after the working electrode was placed into the electrolyte. Methods for electrode preparation and RDE protocols were followed from a previously reported work.[39]

A stock solution was prepared by mixing 0.4 mL of Nafion suspension (Aldrich, 5 wt %, 1100 g equivalent weight), 20 mL of isopropanol (HPLC), and 79.6 mL ultra-pure water (≥18 MΩ cm). The stock solution was then combined with ethylene glycol (99.5%) in a 70/30 composition to make an ink solution. Catalyst inks were prepared by weighing approximately 5 mg of TiO_2-N800-Ir into a 20 mL vial and combining it with the ink solution to reach a concentration of 1 mg_{cat}/mL. The inks were sonicated (Fisher, 40 kHz) for 20 minutes, immersed in a 25 °C bath for 1 minute, and then deposited onto a cleaned gold RDE immediately. Typically, 10 uL of the catalyst ink was deposited onto

the electrode and then spun at 700 RPM on an inverted rotor (Pine MSR electrode rotator) for 10 minutes to ensure even casting. The electrode was then placed in a vacuum oven at 50 °C for 20 minutes.

A material break-in procedure was performed by cycling potential in the range of 0.05 – 1.0 V_{RHE} for 20 cycles at a rate of 100 mV sec^{-1} to stabilize the catalyst material. The cell was then flooded with carbon monoxide gas for 10 minutes and then purged with argon gas for 16 minutes. Carbon monoxide (CO) stripping was performed by applying potential in the range of 0.1 – 1.2 V_{RHE} for two cycles at a rate of 20 mV sec^{-1}. A catalyst oxidation procedure was performed by cycling potential in the range of 0.1 – 1.5 V_{RHE} for 60 cycles at a rate of 100 mV sec^{-1} with electrode rotation of 2500 RPM. An OER break-in procedure was performed by cycling potential in the range of 1.3 – 1.8 V_{RHE} for ten cycles at a rate of 100 mV sec^{-1} with electrode rotation of 2500 RPM. Linear scan voltammetry (LSV) was performed in the range of 1.3 – 1.8 V_{RHE} at a rate of 20 mV sec^{-1}. Chronoamperometry (CA) was performed in the range of 1.37 – 1.6 V_{RHE} in 60 second intervals at each potential (potential step = 0.01 V) with electrode rotation of 2500 RPM. Following CA tests, cyclic voltammetry (CV) was applied in the range of 0.1 – 1.4 V_{RHE} for five cycles at three different rates; 100, 50, and 20 mV sec^{-1}. An accelerated endurance test (AET) was performed by applying a potential of 1.6 V_{RHE} for 13.5 hours with an electrode rotation speed of 2500 RPM. Following the AET, the electrolyte was rinsed out of the cell and replaced with fresh 0.1 M $HClO_4$ electrolyte, hydrogen was again produced on the reference electrode, and the cell was flooded with argon gas for ten

minutes after placing the working electrode back into the cell. CV, LSV, and CA measurements were again performed in the same manner as above.

3. RESULTS AND DISCUSSION

3.1 Synthesis and Characterization of Titanium Oxynitride

3.1.1 Synthesis of TiO_xN_y

The synthesis of titanium oxynitride (TiO_xN_y) was synthesized in a two-step process. First, the TiO_2 nanosheets were made then subsequently transformed into TiO_xN_y. High surface area TiO_2 nanosheets were synthesized in a microwave reactor by solution-phase hydrolysis/condensation reactions. This method was adapted from previously reported reaction conditions conducted in an autoclave.[40]

A plausible growth mechanism for titanium oxide is depicted in Figure 10. First in hydrolysis, an aquo ligand loses a proton to form a hydroxo ligand. Next in the condensation step, two titanium hydroxo complexes join to form double hydroxo bridging ligands.[41]

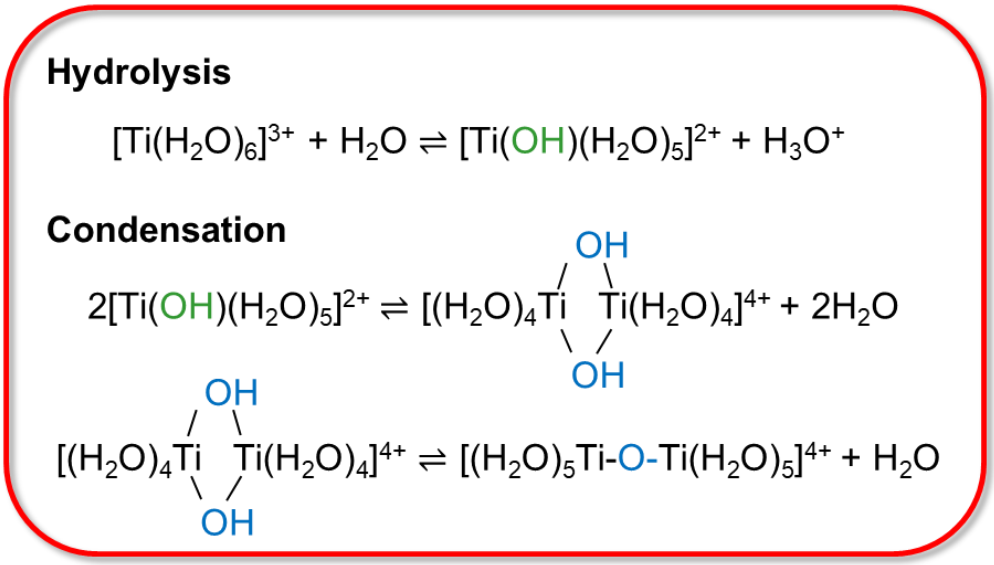

Figure 10. Hydrolysis and condensation reactions for the growth of TiO_2.

For the synthesis of titanium oxide nanosheets, ethylene glycol was used as a coordinating solvent. Ethylene glycol has been utilized in inorganic synthesis as a chelating agent that can potentially coordinate to metals and stabilize nanoparticles after they have formed.[42] Figure 11 shows a simplified diagram of the synthesis of the as prepared titanium oxide and the titanium oxynitride materials.

TiO_2 was transformed into TiO_xN_y by heat treatment in the presence of ammonia. Sample names were then designated as TiO_2-N600 or TiO_2-N800, denoting treatment at 600 ^oC or 800 ^oC respectively. The effect of temperature has been shown to be an important factor in the transformation of TiO_2. Gebauer et al. have observed that titanium oxynitride formation on TiO_2 (P25 Degussa) starts at approximately 700 ^oC.[38] Full nitridation of a nanocrystalline TiO_2 powder has been demonstrated with the same technique by Li et al. by heating at 800 ^oC for five hours with an ammonia flow rate of 1000 mL min^{-1}.[43] Ding et al. have completely transformed TiO_2 nanotubes to TiN nanotubes with a temperature of 900 ^oC.[44] These three studies have all noted that nitridation is facilitated by increased temperature on various TiO_2 morphologies. A plausible chemical reaction for this transformation is as follows:

$$2TiO_2 + 4NH_3 \rightarrow 2\ TiN + 4H_2O + N_2 + 2H_2 \qquad (13)$$

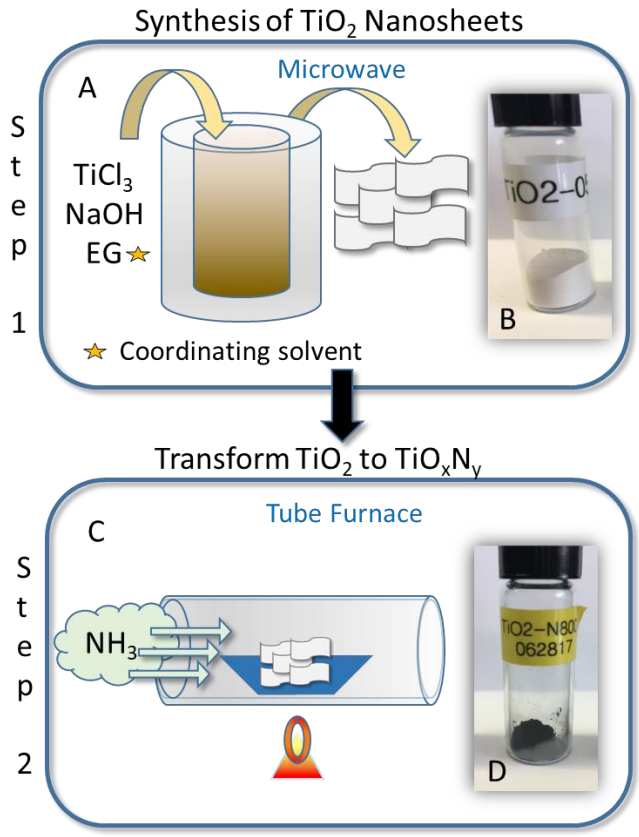

Figure 11. A) Process for synthesis of titanium oxide nanosheets in microwave reactor. B) TiO_2 As-prepared nanosheets dried powder. C) Process for heat treatment in ammonia gas of titanium oxide in tube furnace. D) TiO_2-N800 dried powder.

3.1.2 Characterization of TiO_xN_y

The colors TiO_2-N600 and TiO_2-N800 after heat treatments under ammonia were black (Figure 11D). Color changes have been observed for porous titanium oxynitride sheets by Chen et al.[45] They note a color change was apparent with changing temperature treatments. A change between green, blue, and black were observed for the treatments of 600, 700, and 800 ^oC respectively. No transitional colors were observed for the current

study. Gold colored thin film TiN has been synthesized by Uen et al. by vapor deposition.[46] The observed black color for TiO_2-N600 and TiO_2-N800 is consistent with those observed for titanium oxynitride materials.

The morphology of TiO_2-N600 and TiO_2-N800 were evaluated with scanning electron microscopy. Figure 12A shows that the as-prepared TiO_2 material has a layered sheet-like morphology. The sample TiO_2-N600 (Figure 12B) appears to show some signs of morphological collapse compared to the TiO_2 nanosheet in Figure 12A. The material heated to 800 ^oC (Figure 12C) shows a much more dramatic change in the morphology; the sheet-like quality is gone but there still appears to be a network of particles present.

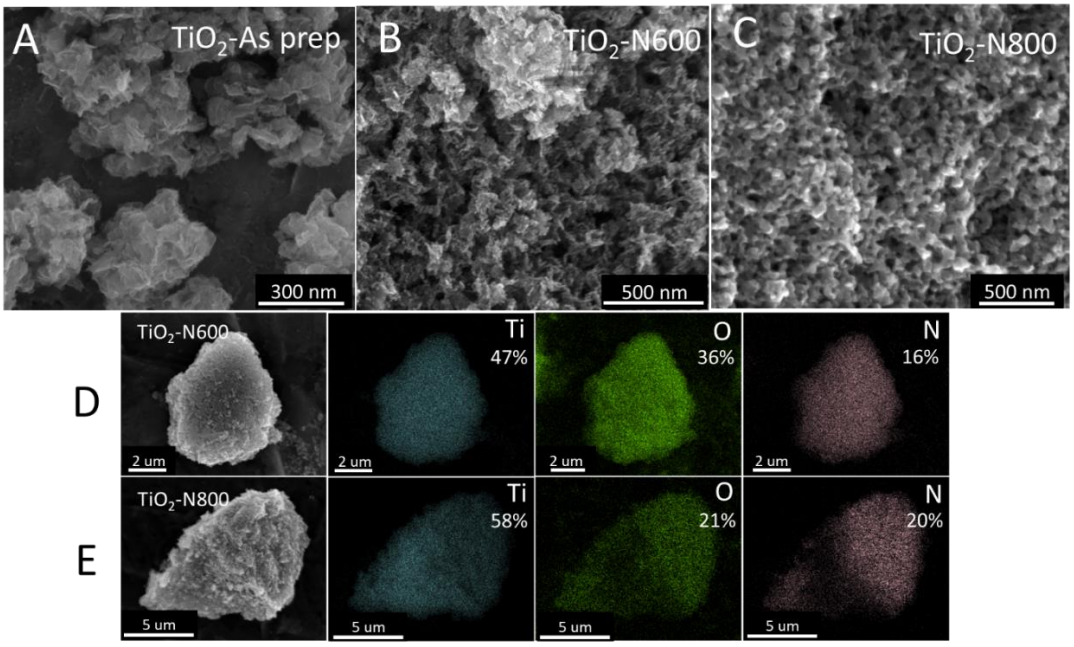

Figure 12. Scanning electron microscopy of A) TiO_2-As prep B) TiO_2-N600 and C) TiO_2-N800. Electron dispersive spectroscopy of D) TiO_2-600 and E) TiO_2-N800. Numbers below elemental symbols are estimated weight percentages.

Energy dispersive spectroscopy (EDS) was used to determine the elemental composition and distribution for TiO_2-N600 and TiO_2-N800. Figure 12D and 12E show the distribution for all three elements titanium, oxygen, and nitrogen. An approximation for the molecular stoichiometry for TiO_xN_y was calculated from the weight percentages provided by EDS. Calculation of titanium, oxygen, and nitrogen was 1, 2.3, and 1.2 respectively for TiO_2-N600. TiO_2-N800 calculation for titanium, oxygen and nitrogen was 1, 1.1, and 1.2 respectively. The approximated values give stoichiometries for TiO_2-N600 and TiO_2-N800 of TiO_2N and TiON respectively. Relative to the amount of titanium, the amount of oxygen was reduced by approximately half by using a higher temperature of 800 ^oC for nitridation.

X-ray diffraction was utilized to determine the phase of the materials synthesized. Generated copper Kα x-ray waves penetrate the surveyed material and are diffracted towards a detector. Constructive and destructive interference is explained by the Bragg equation:

$$2d\sin(\theta) = n\lambda \quad (14)$$

where d is the interlayer distance, θ is the angle of diffraction, n is some integer value, and λ is the wavelength of incoming radiation.

X-ray diffraction (Figure 13A) conducted on the TiO_2 nanosheets and the two heat treated samples, TiO_2-N600 and TiO_2-N800, show significant changes due to the thermal treatments. The TiO_2 nanosheet material showed only two weak diffraction planes, anatase 101 and rutile 110 for titanium oxide. The sample TiO_2-N600 has several

anatase planes (101, 103, 200, and 213) and one rutile plane 211. Chen et al. have observed the presence of both phases in the applied temperature range.[47] The peak at approximately 37° indicates the possible formation of a TiN phase. Gebauer et al. note that at lower ammonia flow rates (42-250 mL min^{-1}) samples heated at 800 °C for 2 hours still maintained rutile TiO_2 diffraction peaks.[38] Considering a low ammonia flow rate (~40 mL/min), the result is inconsistent with the XRD of the current study where anatase and rutile peaks for TiO_2 are no longer expressed in the TiO_2-N800 sample. This is possibly attributed to the differences of the starting TiO_2 materials. Gebauer's starting material had a relatively low surface area of 50 m^2 g^{-1} compared to the high surface area (430 m^2 g^{-1}) nanosheet that was used in this study. The sample TiO_2-800 displays diffraction planes (111, 200, and 220) consistent with the TiN powder diffraction reference. The set of three graphs (Figure 13B-D) display the main diffraction peaks for the sample TiO_2-N800. Close inspection of the peaks with the reference lines for TiN (black) show that the diffraction pattern was slightly shifted to higher angles. Incorporation of oxygen into a titanium nitride lattice has been associated with these angle shifts by Gebauer.[38] This reasoning is also consistent with the elemental composition observed from the EDS for the sample TiO_2-N800.

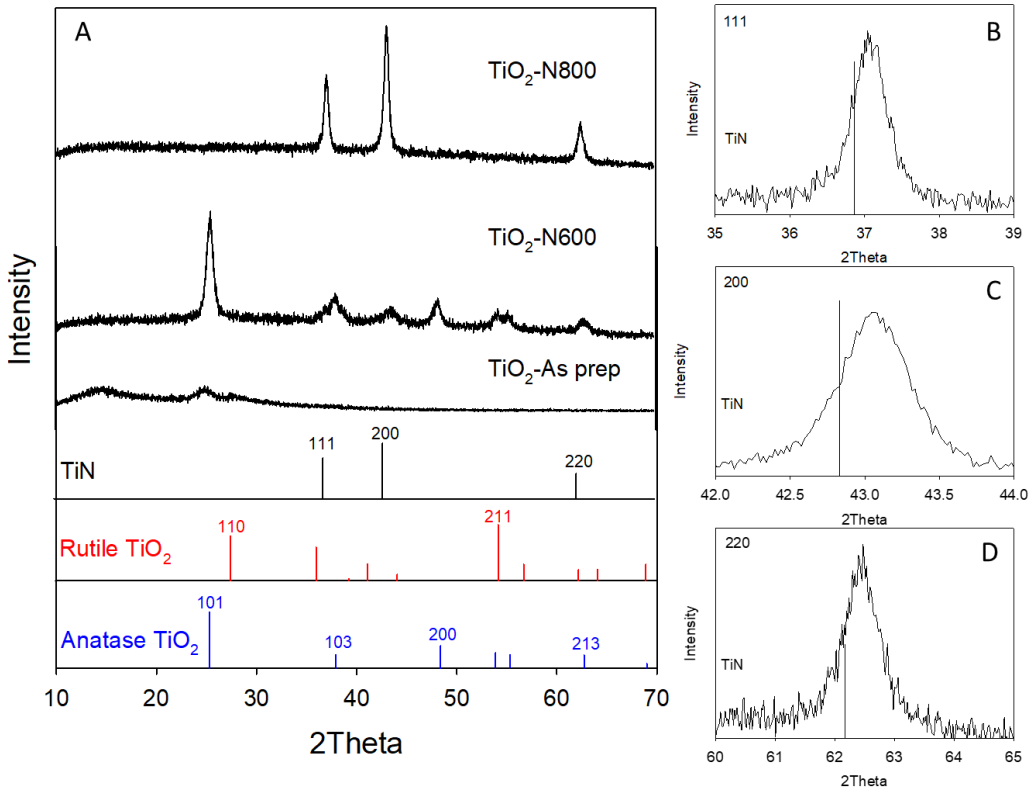

Figure 13. A) X-ray diffraction of as prepared TiO_2 and two heat treatments in ammonia gas, TiO_2-N600 and TiO_2-N800. Shown in an expanded view are peaks of TiO_2-N800 for the planes B) 111, C) 200, and D) 220 peaks for TiO_2-N800. Vertical lines below represent reference peaks for titanium nitride (black), rutile TiO_2 (red), and anatase TiO_2 (blue).

Table 1 has listed data concerning the sample TiO_2-N800 and the references TiN and TiO. The data shows that there is only a fraction of percent difference between the 2Theta values of TiO and TiO_2-N800.

Table 1. Diffraction data for TiO_2-N800 and reference TiN (PDF01-087-0630).

Sample	111		200		220	
	2Theta (2θ)	d-spacing (Å)	2Theta (2θ)	d-spacing (Å)	2Theta (2θ)	d-spacing (Å)
TiN	36.862	2.4364	42.824	2.1100	62.167	1.4920
TiO_2-N800	37.074	2.4230	43.063	2.0980	62.429	1.4860

Given similar 2θ^o values for TiO2-N800 and the TiN reference, it is considered that TiO_2-N800 also has a cubic structure like TiN, as can be seen in Figure 14. The lattice constant (a_o) of a unit cell can be found from the d value (in angstroms) and the indexed plane values (hkl) with the equation for a cubic structure is

$$a_o = d\ x\ \sqrt{h^2 + k^2 + l^2} \tag{15}$$

The lattice constant for the sample TiO_2-N800 was calculated, using the (111) peak, to be 4.196 Å. Chen et al. have calculated lattice constants of 4.196 Å and 4.224 Å for titanium oxynitrides heated to 700 ^{o}C and 800 ^{o}C.[45] Based on the stoichiometry calculated from the EDS and the evaluated XRD data, it is reasonable that TiO_2-N800 is a single TiON cubic phase with nitrogen and oxygen incorporated in the structure.

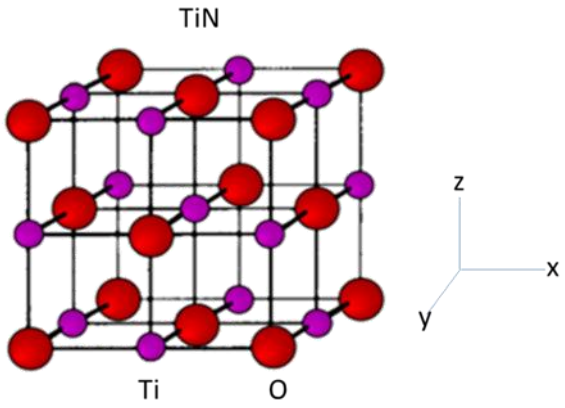

Figure 14. Crystal structure of cubic TiN.[48]

The electronic conductivity was measured to observe the changes induced by thermal treatments. The electronic conductivity of TiO_xN_y materials are directly associated with the nitrogen and oxygen content. Williams et al. recorded increased resistivity for a TiN thin film as it adsorbed oxygen.[49] Similarly, the estimated stoichiometries of TiO_2N and TiON for TiO_2-N600 and TiO_2-N800 demonstrate the change in oxygen content in the current study. Electronic conductivity of the as prepared TiO_2 nanosheets and the two heat treated samples were measured (Table 1). The conductivity of the TiO_2 nanosheet was so low that it can be described as an insulator. An intermediate conductivity of 1.3×10^{-4} S cm^{-1} was measured for the sample TiO_2-N600. The sample TiO_2-N800 had a seven-magnitude improvement in conductivity to 1.4×10^{-1} S cm^{-1} compared with the starting TiO_2 nanosheet material. The heat and ammonia treatment promoted the electronic conductivity of the as prepared material from an insulator to a semiconductor. The electronic conductivity of TiO_2-N800 is now within

the previously reported value (0.1 S cm^{-1}) for reasonable electrical conductivity of an electrocatalyst support material.[10]

The BET surface area (Table 2) of the as prepared TiO_2 nanosheets were relatively high, 433 m^2 g^{-1}. Collapse of the original morphology is apparent in Figures 12A-C as the material was heated, leading to dramatic changes in the surface area. Platinum supporting TiN for fuel cells have been synthesized with a surface area of 40-55 m^2 g^{-1} by Avasarala et al.[37] Heating of the TiO_2 nanosheets caused a decrease in the surface area down to 54 m^2 g^{-1} for the sample TiO_2-N800. This surface area is still sufficient for use as a support material for an electrocatalyst. Moreover, TiO_2-N800, was selected for use a support material because of its complimentary surface area and electronic conductivity.

Table 2. Surface Area and Conductivity Measurements

Sample	σ (S cm^{-1})	m^2 g^{-1}
TiO_2-As prep	4.8 x 10^{-8}	433
TiO_2-N600	1.3 x 10^{-4}	138
TiO_2-N800	1.4 x 10^{-1}	54

3.2 Synthesis and Characterization of Titanium Oxynitride Supported Iridium

3.2.1 Synthesis of Titanium Oxynitride Supported Iridium

Solvothermal synthesis that employs ethylene glycol (EG) as a reducing agent for metal compounds have been widely used. Gold and silver nanoparticles have been produced with shape control by Sun and Xia.[50] Noble metals such as platinum, rhodium, and palladium, have been reduced to create nanoparticles by Hei et al.[51] Size control of

iridium and ruthenium nanoparticles have been achieved by Nguyen et al. using polyvinylpyrrolidone (PVP), a capping agent, and EG as reducing agent and solvent.[52]

To deposit iridium onto the support material, TiO_2-N800 and the catalyst precursor ($IrCl_3 \cdot xH_2O$) were dispersed into ethylene glycol and heated in a microwave reactor (Figure 15). The resultant material was given the sample name TiO_2-N800-Ir. The dried powder of TiO_2-N800-Ir in Figure 15B has a very similar black color as the TiO_2-N600 and TiO_2-N800 material.

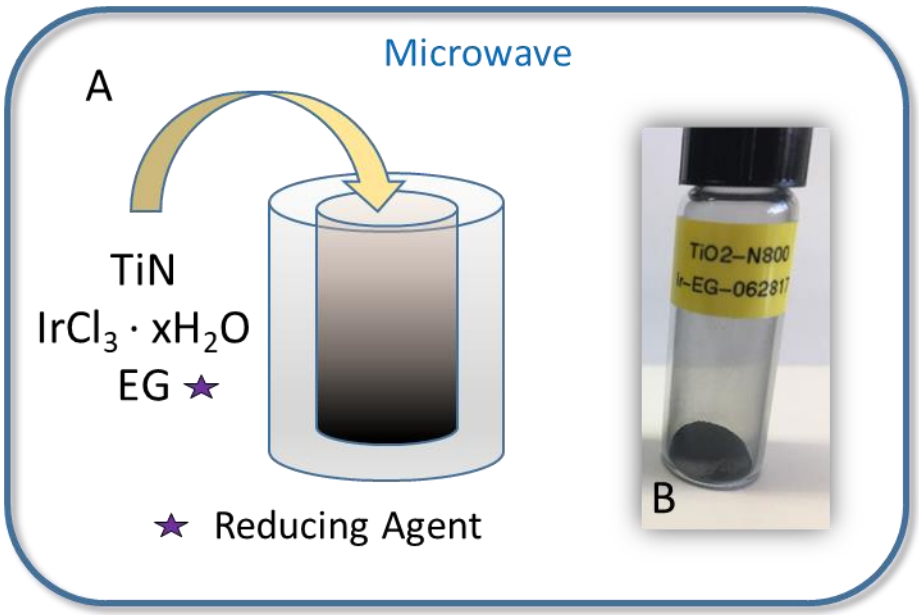

Figure 15. A) Synthesis of TiO_2-N800-Ir in microwave. B) Dried powder of TiO_2-N800-Ir.

3.2.2 Characterization of Titanium Oxynitride Supported Iridium

Electron dispersive spectroscopy was performed on TiO_2-N800-Ir to validate that iridium had been deposited onto the support material. The presence and uniform

distribution of iridium is evident in Figure 16F. The density of iridium skews the relative weight percent in its favor over the less dense oxygen and nitrogen. The atomic percentage of iridium was much lower, only five percent. The comparison of weight and atomic percentages is listed in Table 3. Scanning electron microscopy of TiO_2-N800-Ir in Figure 16D shows that the morphology of the material, a network of nanoparticles, has not changed when compared to TiO_2-N800 (Figure 12C).

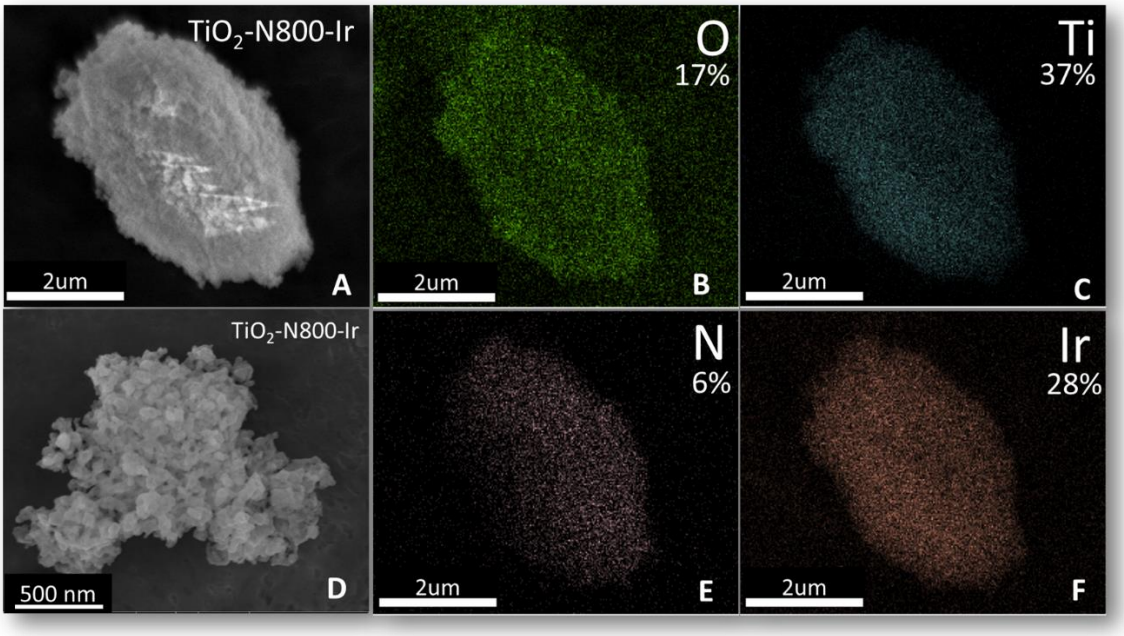

Figure 16. Electron dispersive spectroscopy of A) TiO2-N800-Ir with the following elements detected: B) oxygen C) titanium E) nitrogen and F) iridium. SEM image of D) TiO2-N800-Ir. Numbers below elemental symbols are estimated weight percentages.

Table 3. Weight percent and atomic percent values for elemental mapping of TiO2-N800-Ir from electron dispersive spectroscopy featured in Figure 16.

Element	Weight %	Atomic %
Avg N%	6	14
Avg O%	17	32
Avg Ti%	37	27
Avg Ir%	28	5

Figure 17A shows the XRD pattern for the samples TiO_2-N800 and TiO_2-N800-Ir, as well as powder diffraction references. Similar peaks were observed for TiO_2-N800-Ir after the deposition of iridium. No distinct diffraction planes were detected for metallic or oxide phases of iridium. However, the EDS experiment detected a significant amount of iridium present within the sample. The lack of iridium diffraction planes suggests that the deposited iridium is not a highly ordered crystalline structure but rather an amorphous phase or small cluster. Metallic iridium was previously deposited in another study, and was observed to have low crystallinity, but when it is heated in air it transformed to a highly ordered rutile iridium oxide.[52]

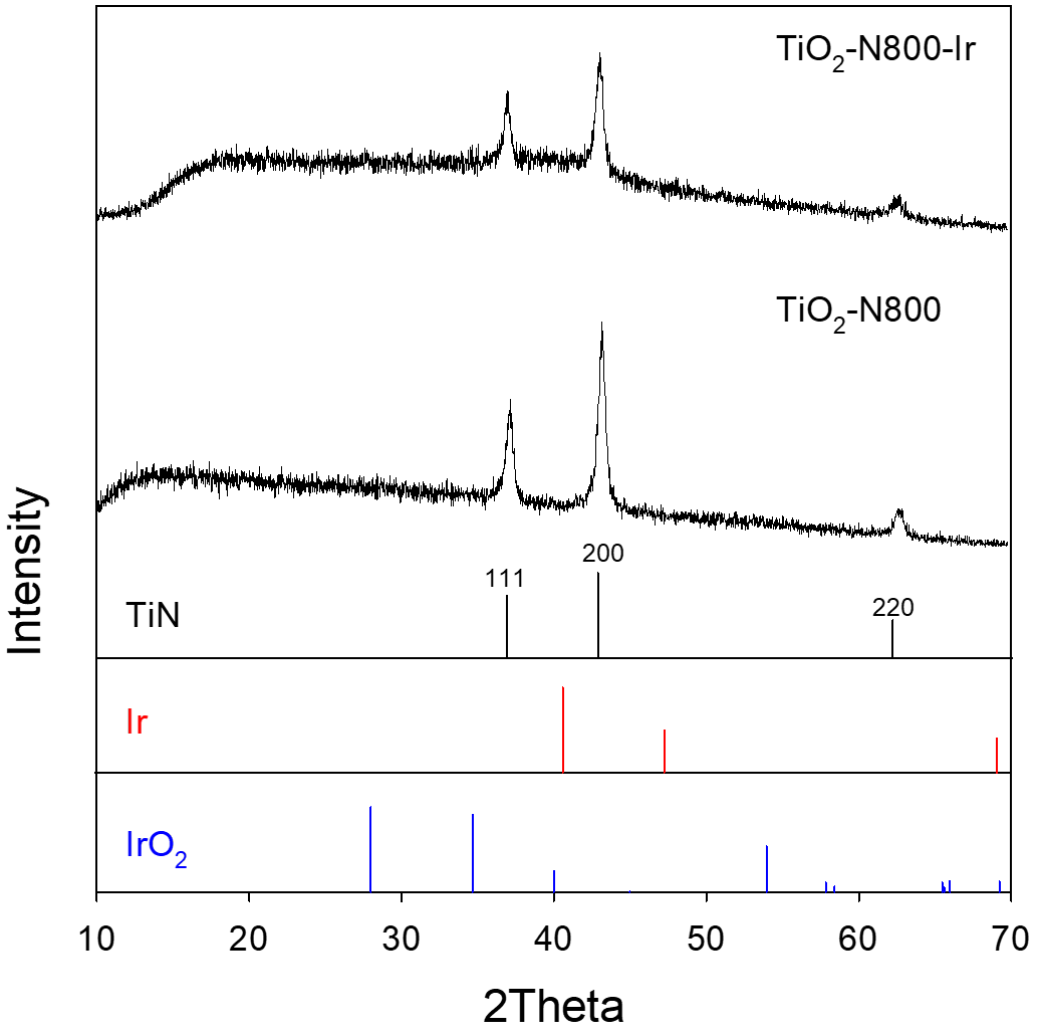

Figure 17. X-ray diffraction of TiO_2-N800 and TiO_2-N800-Ir. Vertical lines below represent reference peaks for TiN (black), rutile TiO_2 (red), and anatase TiO_2 (blue).

3.3 Electrochemical Characterization

3.3.1 Cyclic Voltammetry at Low Potential Range

Cyclic voltammetry at low potential range (0.05-1.0 V_{RHE}) was performed for TiO_2-N800 and TiO_2-N800-Ir. Figure 18 shows the CV (2^{nd} and 20^{th} cycles) of the

support material, TiO_2-N800, which shows a capacitive response consistent with double layer capacitance or pseudo capacitance. No features consistent with irreversible material oxidation were observed within this potential range. Little to no change is evident between the second and twentieth cycle.

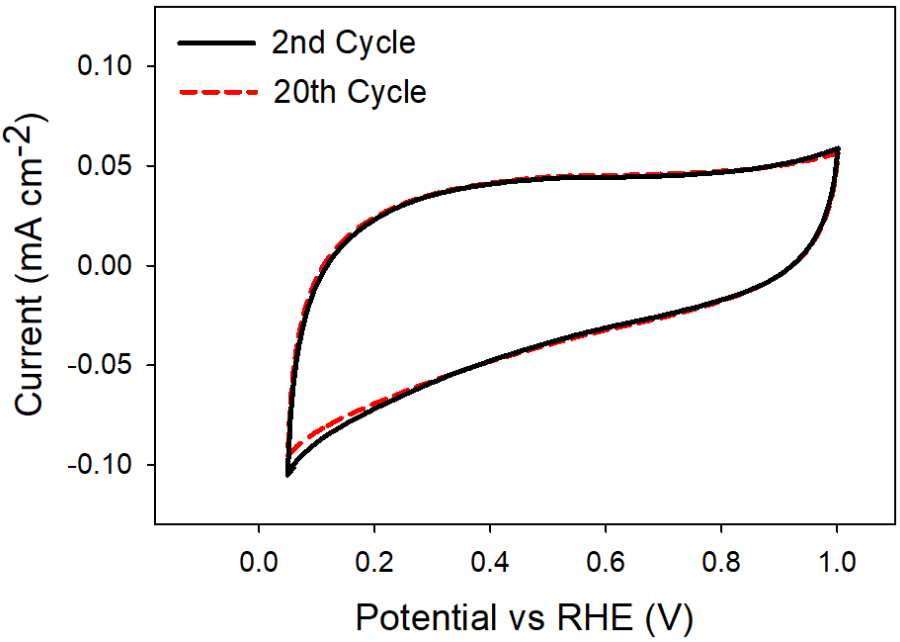

Figure 18. CV of support material, TiO_2-N800, showing the 2nd and 20th cycle at a rate of 100 mV sec^{-1} in 0.1 $HClO_4$.

Electrochemical studies have noted that hydrogen is able to absorb onto many metallic surfaces.[53] The direction of potential movement or scan can be referred to as oxidative sweep (positive direction) or reductive sweep (negative sweep). For TiO_2-N800-Ir, hydrogen adsorption on the reductive sweep and hydrogen desorption on the oxidative sweep in Figure 19 was apparent in the range of 0.0-0.2 V_{RHE}, which supports

that the metallic iridium had been deposited. Capacitance from the support material had a very small contribution by comparison of the Y-axis range in Figure 19.

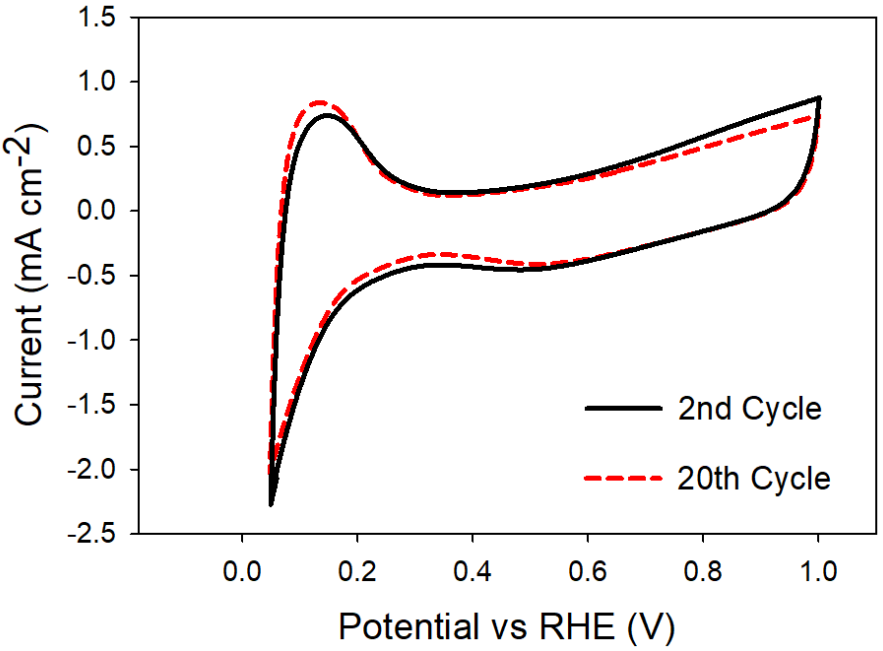

Figure 19. Cyclic voltammetry, 20 cycles at a rate of 100 mV sec^{-1} in 0.1 M perchloric acid for TiO_2-N800-Ir.

3.3.2 Carbon Monoxide Stripping

Carbon monoxide (CO) stripping is an electrochemical test used to calculate the electrochemical surface area (ECSA) of metallic species. CO binds strongly to metallic surface atoms but can be electrochemically released in a known potential range.[54] The overall reaction[55] for removing adsorbed CO is:

$$CO_{ads} + H_2O \rightarrow CO_2 + 2H^+ + 2e^- \quad (16)$$

The detection of a CO oxidation peak further supports the presence of a metallic iridium phase. The electrochemical surface area of metallic iridium ($ECSA_{Ir}$) was calculated using the equations:

$$Q_{CO}\ (C) = \frac{\int_a^b i\ dV}{dV/dt} \tag{17}$$

$$ECSA_{Ir}(m^2 g_{Ir}^{-1}) = \left[\frac{Q_{CO}\ (C)}{358\ \mu C\ cm_{Ir}^{-2}\ \ L_{Ir}(mg_{Ir}\ cm^{-2})A_g(cm^2)}\right] 10^5 \tag{18}$$

The total charge, $Q_{CO}\ (C)$, is calculated from the integrated CO oxidation ($\int_a^b i\ dV$) divided by the scan rate (dV/dt) applied. In equation 17, i is the current in Amps. Figure 20 shows the CO stripping voltammetry of TiO_2-N800-Ir. The CO oxidation is collected from the integrated peak (~0.7-1.1V) in the CV highlighted by the red dashed line. The experimentally found value, 358 μC cm_{Ir}^{-2}, for the electric charge associated with the release of CO on polycrystalline iridium was used as a best estimate for the metallic iridium species in this study.[56] The calculated $ECSA_{Ir}$ of metallic iridium was 125 ± 19 $m^2\ g_{Ir}^{-1}$, which was high compared to other studies. Prior evaluations of ECSA by mercury adsorption by Alia et al. have calculated 29.4 $m^2\ g_{Ir}^{-1}$ for metallic iridium and 28.7 $m^2\ g_{Ir}^{-1}$ for iridium oxide nanoparticle.[56] Alia also evaluated the $ECSA_{Ir}$ by CO adsorption and calculated a reasonably close figure of 30.8 $m^2\ g_{Ir}^{-1}$. To this end, we assume that the evaluated $ECSA_{Ir}$ of metallic iridium is a close approximation for the ECSA of an iridium oxide active catalyst. This comparison is important because metallic iridium was converted to iridium oxide, as will be explained in the forthcoming section.

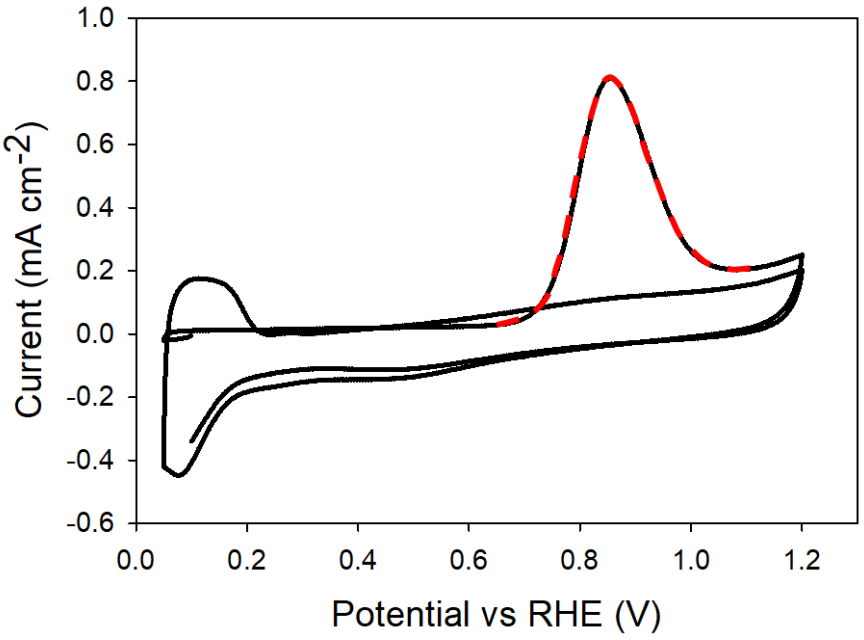

Figure 20. Carbon monoxide stripping of TiO_2-N800-Ir at a rate of 20 mV sec^{-1} in 0.1 M perchloric acid and the dashed red line shows the integrated peak.

3.3.3 Oxidation of Catalyst and Support by Cyclic Voltammetry

For the electrochemical evaluation of the catalyst, TiO_2-N800-Ir was cast onto a gold electrode. The remaining electrochemical test were performed in wider potential ranges, so it is important to know how the bare electrode will respond electrochemically. A CV of the bare gold electrode is shown in Figure 21. A broad oxidation peak is noted to take place at approximately 1.4 V_{RHE}. A sharp reductive peak is noticed at approximately 1.2 V_{RHE}. This general shape and position of Au redox peaks are consistent with a prior study in the literature.[57]

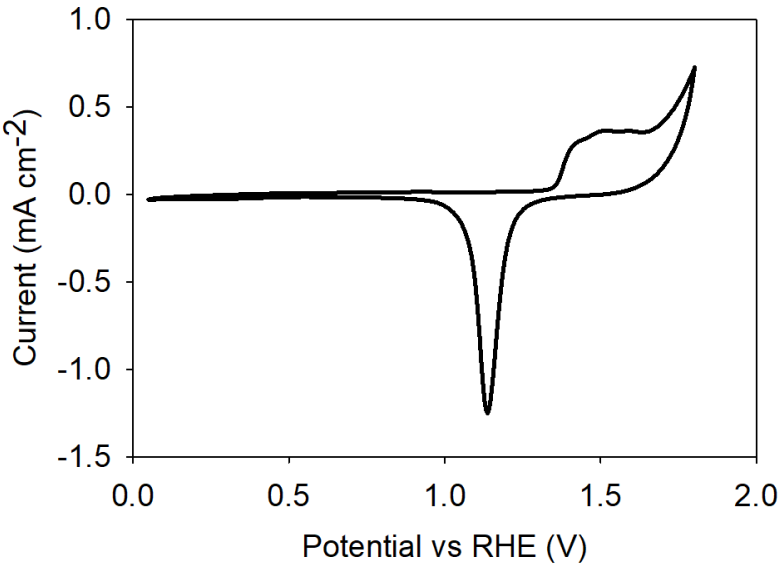

Figure 21. Cyclic voltammetry of the bare gold electrode in 0.1 $HClO_4$ taken at 100 mV s^{-1}.

Cyclic voltammetry was performed on the support material, TiO_2-N800. The black and red lines in Figure 22 are the 1st and 60th cycle respectively. The CV shows an irreversible oxidation at approximately 1.3 V_{RHE} which is consistent with prior electrochemical testing on titanium oxynitride materials.[38] Oxidation of the support is typically undesirable for the activity and stability of the overall catalyst. Support oxidation that leads to reduction in catalyst activity is called support passivation.[8] The interaction between the support and the active catalyst can become weakened and lead to mass loss. An oxidized support can also grow into the catalyst layer and change catalytic properties. In addition, the conductivity of the support material can be changed with increased oxidation and weaken the applied potential to the catalyst site thus nulling its

effect. The redox peaks from the gold electrode can still be seen at the expected potentials, 1.2 and 1.4 V_{RHE}.

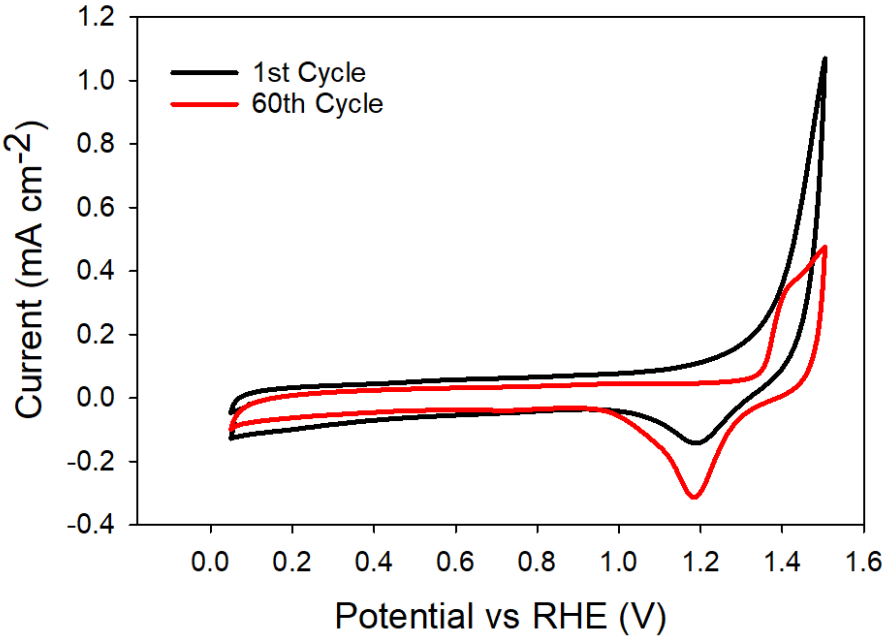

Figure 22. Electrochemical oxidation of support material TiO_2-N800 in 0.1 $HClO_4$ taken at 100 mV s^{-1} for sixty cycles.

Cyclic voltammetry was performed on TiO_2-N800-Ir to oxidize the metallic iridium. Figure 23 shows TiO_2-N800-Ir at the 1st cycle (in black) and the 60th cycle (in red). Hydrogen adsorption/desorption can still be seen the voltage range 0.0-0.2 V_{RHE} for the 1st cycle whereas this feature has been lost in the 60th cycle which indicates the change from metallic iridium to iridium oxide. Oxidation features become more distinct between the ranges of 0.9-1.3 V_{RHE} when comparing the 1st and 60th cycles. Juodkazyte et al. have reported these oxidation peaks and include the following reversible chemical equations[58]:

$$Ir + 3H_2O \Leftrightarrow Ir(OH)_3 + 3H^+ + 3e^- \quad (19)$$

$$Ir + (n+2)H_2O \Leftrightarrow IrO_2 \cdot nH_2O + 4H^+ + 4e^- \quad (20)$$

The first feature seen in the 60th cycle at approximately 0.9 V_{RHE} is associated with the metallic iridium oxidation to an Ir(III) species. The second feature seen at approximately 1.2 V_{RHE} is associated with oxidation to a hydrous Ir(IV) oxide. The reduction peak associated with the reduction of IrO_2 is observed at approximately at 0.8 V_{RHE} in the negative scan direction. The irreversible oxidation of the support material is observed at approximately 1.3 V_{RHE}. After this oxidation process, the catalyst will now be referred to as TiO_2-N800-Ir-EO, where EO stands for electrochemical oxidation.

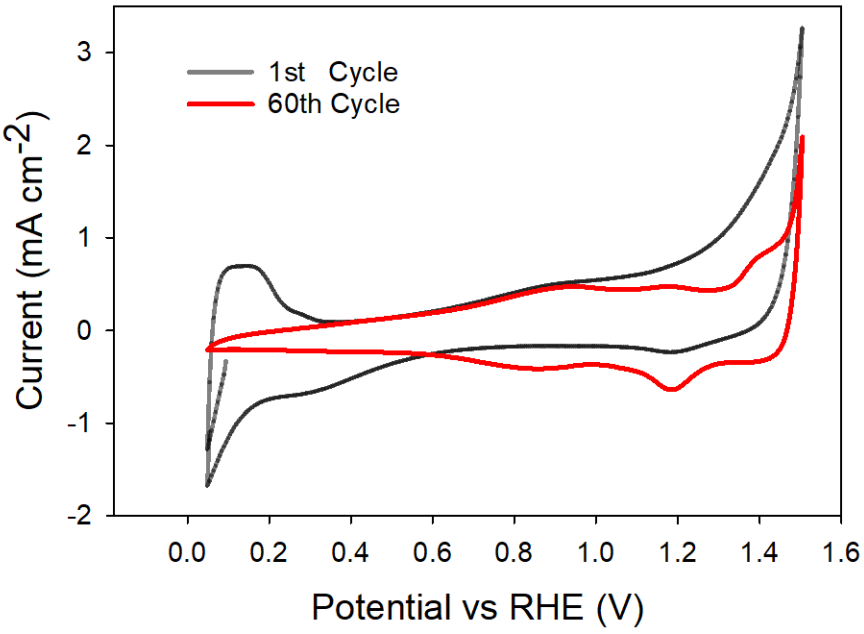

Figure 23. Electrochemical oxidation of A) TiO_2-N800-Ir for 60 cycles at a rate of 100 mV sec^{-1} in 0.1 M perchloric acid.

3.3.4 Oxygen Evolution Activity of Titanium Oxynitride Supported Iridium Oxide Electrocatalyst

Oxygen evolution activity of TiO_2-N800-Ir-EO was determined by chronoamperometry (CA) test. Figure 24 shows the initial mass-normalized activity of TiO_2-N800-Ir-EO compared to that of an iridium oxide standard bulk material purchased from Alpha Aesar (IrO_2-AA). The voltage was held at a specific potential for a given interval. Applied potentials ranged from 1.36-1.57 V_{RHE} with a 0.01 V_{RHE} step. The collected time at a given potential was adjusted to verify that the current response reached a steady state. Data for standard iridium oxide was provided by a prior study.[59] OER activity for both materials is nearly zero up to 1.46 V_{RHE}. Activity begins for TiO_2-N800-Ir-EO at 1.47 V_{RHE} somewhat ahead of the standard material. Above 1.5 V_{RHE}, the activity of TiO_2-N800-Ir-EO begins to depart from that of IrO_2-AA by a large margin.

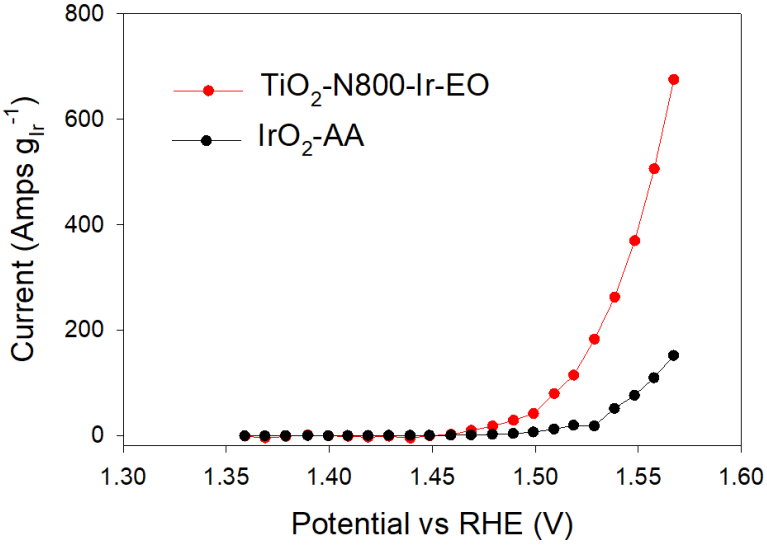

Figure 24. Initial chronoamperometry of TiO_2-N800-Ir-EO and standard IrO_2-AA. Values for IrO_2-AA provided by prior work.[59]

The Tafel plot in Figure 25 was constructed from mass normalized data points in the CA test. While points in the CA data set range from 1.37-1.57V, the selected points for making the Tafel plot were limited to those that maintain a linear response. The slope (b) of the Tafel plot is represented with the following equation:

$$b = \frac{\partial \eta}{\partial \log(i)} = \frac{2.303RT}{\alpha F} \quad (21)$$

where α is the transfer coefficient for the anodic reaction, η is the ohmic-drop corrected overpotential, F is Faraday's constant, R is the gas constant, and T is the temperature.[60] Mass transport and other variables that lie outside the kinetic barriers of the OER reaction can make this response non-linear. Determining the activity of a given catalyst within this linear response ensures that materials are evaluated with as few other limiting factors as possible.

The Tafel slope is a commonly used factor for evaluating the activity of an electrocatalyst. It intimates how much potential needs be applied to produce a resultant amount of current. The Tafel slope also can give some mechanistic insight to the catalyzed reaction at the electrode. It is noted in equation 19 the slope is dependent on α, the transfer coefficient.[60] The transfer coefficient of a RDS in a multi-step mechanism can be expressed as:

$$\alpha = \frac{n_f}{\nu} + n_r\beta \tag{22}$$

where n_f is the number of electrons transferred prior to the RDS, ν is the number of times the RDS occurs in one mechanistic cycle, n_r is the number of electrons transferred in a RDS, and β is a symmetry factor (usually approximated to 0.5[61]). The value n_r is one for any RDS that is not a chemical process; for a chemical process the value is zero. Appling these parameters:

$$\alpha(RDS_1) = \frac{0}{1} + 1(0.5) = 0.5 \tag{23}$$

$$\alpha(\mathrm{RDS}_2) = \frac{1}{1} + 1(0.5) = 1.5 \tag{24}$$

$$\alpha(\mathrm{RDS}_{Chem}) = \frac{1}{1} + 0(0.5) = 1 \tag{25}$$

When the transfer coefficient is now substituted into equation 19, an approximated slope is found for each RDS. The Tafel slopes calculated from the transfer coefficients $\alpha(RDS_1)$, $\alpha(RDS_2)$, and $\alpha(RDS_3)$ are 120, 40, and 60mV dec^{-1} respectively. In this study, the Tafel slope of TiO_2-N800-Ir-EO was determined to be 43 mV dec^{-1}. A slope of 35

mV dec^{-1} was determined for the standard material.[59] Referring back to the four commonly accepted mechanisms (Figure 6) [10], paths 1 and 2 both have no electron transfer steps preceded by another, so their likelihood is ruled out. Paths 3 and 4 both fit the parameters as a possible mechanism because they have concurrent electron transfer steps. The analysis of the Tafel slope therefore supports that oxygen evolution by TiO_2-N800-Ir-EO proceeds by either the "electrochemical oxide path" or the "DFT-predicted oxide path" and the second electron transfer in the process is the rate determining step in the reaction. Tafel slopes of approximately 60 mV dec^{-1} for bulk and nanoparticle iridium oxide have been reported by Reier et al.[16] Oh et al. also report 60 mV dec^{-1} on supported iridium oxide nanoparticles.[22] Antolini has observed Tafel slopes ranging from 36-42 mV dec^{-1} with the variance of tin doping in iridium oxides.[62] These values from the literature suggest that both the activity and the mechanism responsible for OER are very sensitive to the catalyst composition and interaction with the local environment.

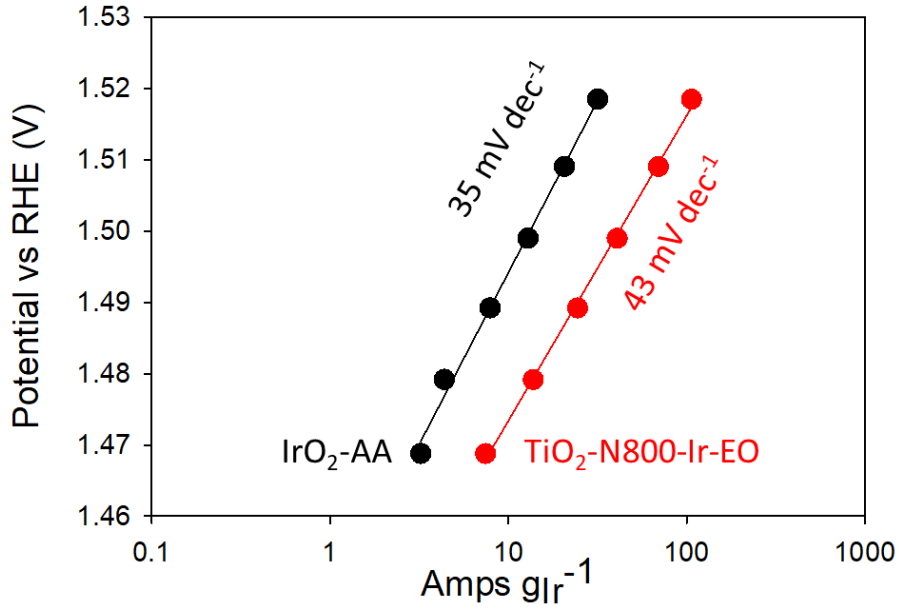

Figure 25. Tafel plots for TiO_2-N800-Ir-EO and IrO_2-AA derived from chronoamperometry measurement; potential range of 1.47-1.52 V. Values for IrO_2-AA provided by prior work.[59]

The initial mass normalized activity of the tested catalyst, TiO_2-N800-Ir-EO, was compared with that of the standard material, IrO_2-AA, in Figure 26. The current for these values were obtained at 1.51 V_{RHE} from the CA test to avoid non-kinetic factors contributing to the OER activity. The initial activity of TiO_2-N800-Ir-EO (75 A g_{Ir}^{-1}) was approximately six times larger than that of the standard material (11.6 A g_{Ir}^{-1}). The standard deviation of the catalyst was also roughly three times the standard deviation of the catalyst, which may arise from a difference in the electrode layer. Specific activity was calculated by dividing the mass normalized current of iridium oxide by the ECSA of

metallic iridium. The specific activity of the active catalyst was calculated to be 6.81 uA cm^{-2}.

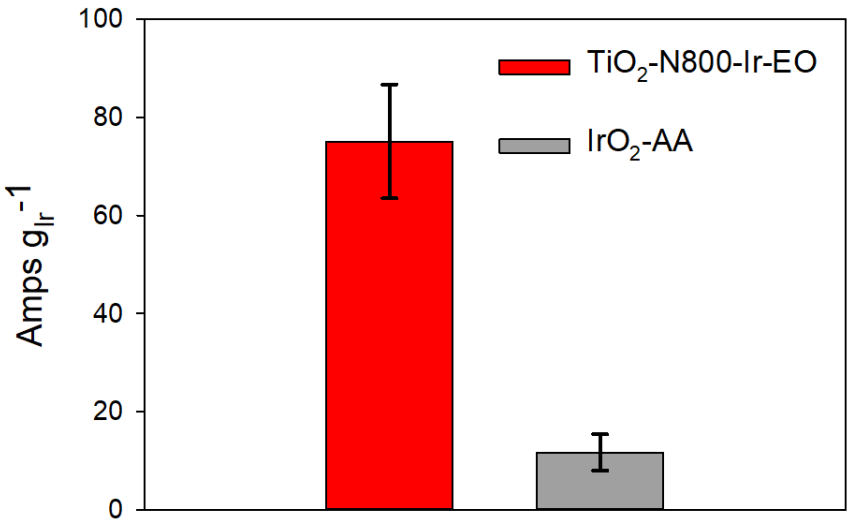

Figure 26. Bar graph showing the initial mass activity comparison of TiO_2-N800-Ir-EO and standard IrO_2-AA before accelerated endurance testing. Values for IrO_2-AA provided by prior work.[59]

There is a lot of varied work in the field of electrocatalysts for water splitting, so comparisons of derived activity should come from similar conditions for reliability. The potential at which a current is measured for catalyst activity can be variable depending on the apparent Tafel plot linearity for a given catalyst. Linear scanning voltammetry has been used in the past, but it has since been recognized to add capacitance contributions to the recorded current.[59] Measurement in differing electrolytes can have dramatic effects on current response as well. MEA and RDE can have vast differences in activities for the same catalyst material.[63] In a similar supported iridium electrocatalyst study, Lu et al. have reported IrO_2 on TiO_2 nanotubes to have an initial mass activity of 32 A g_{Ir}^{-1}.[64]

Iridium nickel on iridium oxide has achieved an initial mass activity of 88 A g_{Ir}^{-1} by Nong et al.[65] Prior work by Godinez et al. have evaluated the initial mass activity at 1.51V of a nickel iridium catalyst to be 220 A g_{Ir}^{-1}.[59] These comparisons show that the activity of TiO_2-N800-Ir-EO was better in the case of supported catalyst but much lower in the case of metal alloys.

3.3.5 Comparing Catalyst Activity and Stability

An accelerated endurance test was applied to TiO_2-N800-Ir-EO and standard IrO_2-AA after data was collected for initial activity. This test is a way to simulate accelerated degradation during the use of a catalyst in practical application. The endurance test held the electrode at a fixed potential (1.6V) for 13.5 hours. The CA test was then performed again to get a measure of the catalyst's stability. Figure 27 shows the plotted CA data for the catalyst material and an iridium oxide standard before and after the stability test. The OER activity of TiO_2-N800-Ir-EO has decreased but is still larger than the standard IrO_2-AA initial activity.

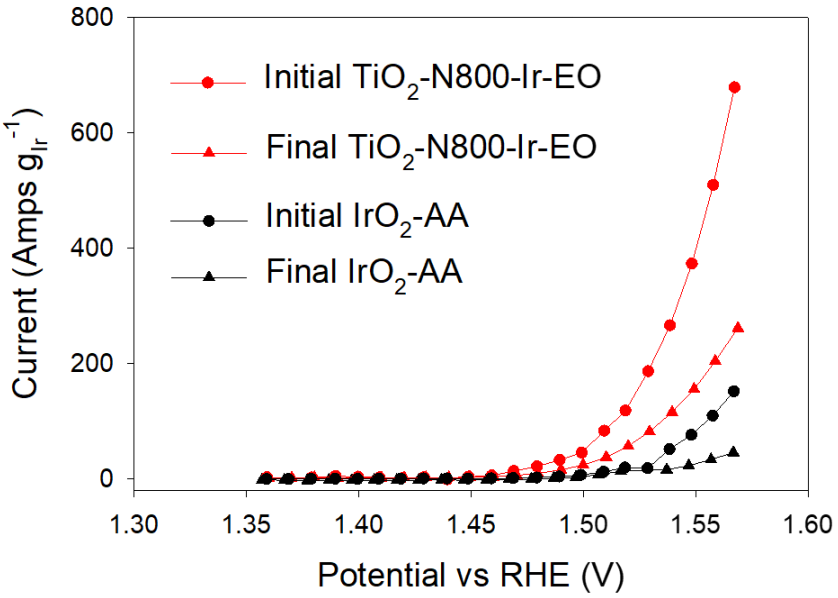

Figure 27. Chronoamperometry of TiO_2-N800-Ir-EO and standard IrO_2-AA before and after endurance test. Values for IrO_2-AA provided by prior work.[59]

Tafel plots were made for both TiO_2-N800-Ir-EO and IrO_2-AA after the accelerated endurance test. Plots were made in the same manner using chronoamperometry data in the same range of 1.47-1.52 V_{RHE}. These plots are combined with the initial Tafel plots for comparison in Figure 28. The calculated Tafel slopes were 48 and 46 mV dec^{-1} for TiO_2-N800-Ir-EO and IrO_2-AA respectively. Comparing the initial and final values, IrO_2-AA had an increase in slope from 36 to 46 mV dec^{-1}, while TiO_2-N800-Ir-EO increased from 43 to 48 mV dec^{-1}. The Tafel slopes for TiO_2-N800-Ir-EO before and after the accelerated endurance test suggests that the mechanism is similar for OER.

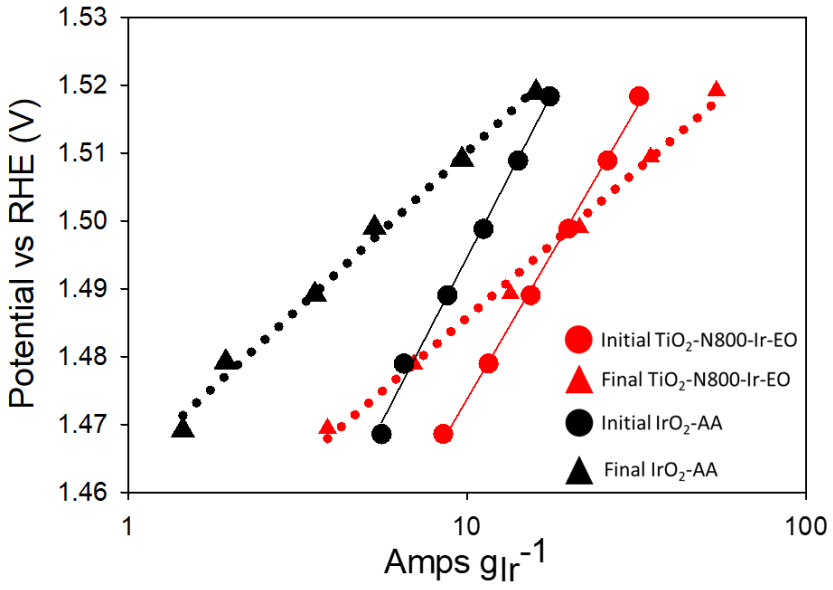

Figure 28. Tafel plots of TiO_2-N800-Ir-EO and standard IrO_2-AA before and after accelerated endurance testing. Values for IrO_2-AA provided by prior work.[59]

The mass normalized activity of TiO_2-N800-Ir-EO and IrO_2-AA before and after the accelerated endurance test are shown in Figure 29. The stability of the catalyst can be compared most easily with this bar graph. The percent of activity retention for TiO_2-N800-Ir-EO and IrO_2-AA are 32 and 72%. From these test, TiO_2-N800-Ir-EO was determined to have issues related to its stability. There are several distinct pathways to catalytic degradation. Support passivation, the oxidation of underlying support materials, has been discussed already. Three other phenomena for activity loss are Ostwald ripening, reprecipitation, and coalescence.[8] Ostwald ripening, also referred to as particle coarsening, is the effect most common with nanoparticle size domains. Dissolved ions from smaller nanoparticles can be redeposited onto large nanoparticles, thus creating an overall larger nanoparticle with reduced exposed catalytic sites. Reprecipitation is the

redeposition of catalyst ions onto the support creating a variance in size distribution of the overall catalyst. Coalescence involves the joining of catalyst particles that are close in proximity to one another. Whenever two or more particles form a new larger particle, the amount available catalytic surface is reduced. Given that the change in activity was quite drastic, it is possible that the catalyst is susceptible to all these degradation pathways, however more analysis is needed to determine the specific cause of degradation. Table 5 has a summary of calculated values for this study.

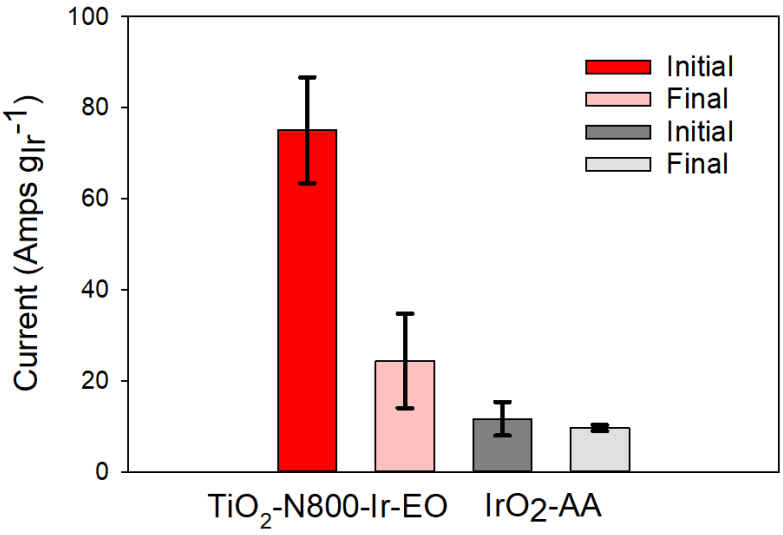

Figure 29. Bar graph showing the mass activity comparison of TiO_2-N800-Ir-EO and standard IrO_2-AA before and after accelerated endurance testing. Values for IrO_2-AA provided by prior work.[59]

Table 4. Comparison of iridium oxide standard from Alpha Aesar with TiO_2-N800-Ir-EO mass and geometric activity normalizations before and after endurance testing. Values for IrO_2-AA provided by prior work.[59]

Value	Parameter	IrO_2-AA	TiO_2-N800-Ir-EO
Loading	Material (μg_{mat} cm^{-2}_{geo})	13.7	50.9
	Iridium (μg_{Ir} cm^{-2}_{geo})	11.6	14.3
$ECSA_{Ir,CO}$ (m^2 g^{-1})		–	125 ± 19
Initial	$J_{geo}^{1.51V}$ (A cm^{-2}_{disk})	0.15 ± 0.04	1.09 ± 0.20
	$J_m^{1.51V}$ (A g_{Ir}^{-1})	11.6 ± 3.7	75 ± 12
	$J_s^{1.51V}$ (A cm^{-2}_{Ir})	-	6.81×10^{-5}
After Durability Testing (1.6 V)	$J_{geo}^{1.51V}$ (A cm^{-2}_{disk})	0.12 ± 0.02	0.36 ± 0.13
	$J_m^{1.51V}$ (A g_{Ir}^{-1})	9.7 ± 0.7	24 ± 10
	$J_s^{1.51V}$ (A cm^{-2}_{Ir})	-	1.94×10^{-5}
Percent OER mass activity (Final/Initial)	AET $J_m^{1.51V}$ / Initial $J_m^{1.51V}$ (%)	72 ± 7	32 ± 17

4. CONCLUSIONS

Titanium oxide nanosheets were synthesized with facile microwave-assisted solvothermal process. The TiO_2 as-prepared nanosheets had a BET surface area of 433 $m^2\ g^{-1}$ and displayed an electronic conductivity of $4.8x10^{-8}$ S cm^{-1}, which is comparable to an insulator. The TiO_2 material was confirmed by SEM to have a nanosheet morphology. Heat treatment of the material under flowing ammonia gas increased the electronic conductivity to $1.3x10^{-4}$ and $1.4x10^{-1}$ S cm^{-1} for heating at 600 and 800 ^oC, respectively. BET surface area of the material changed to 138 $m^2\ g^{-1}$ for TiO_2-N600 and 54 $m^2\ g^{-1}$ for TiO_2-N800. The support material, TiO_2-N800, was observed by SEM to display a nanoparticle network. EDS of TiO_2-N800 showed nitrogen weight percent of 20%. XRD of the support material showed a close match for powder diffraction reference TiN. The stoichiometry based on the observed EDS weight percent of titanium, nitrogen, and oxygen was calculated to be TiON. Based on XRD and EDS observations, there is sufficient evidence to support that TiO2-N800 is a single-phase titanium oxynitride. Ethylene glycol was used to reduce an iridium precursor and deposit metallic iridium onto the conductive support material, TiO_2-N800. The weight percent of deposited iridium, 28%, was detected by EDS and was observed to fair distribution with no agglomeration. No crystalline phases of iridium on the support material after deposition were observed from XRD measurements. These observations from the EDS and XRD support that the iridium has been deposited in either an amorphous manner or that the iridium has been formed into small discrete clusters that are beyond the limit of detection by XRD.

Electrochemical testing of the catalyst, TiO_2-N800-Ir-EO, was performed by RDE measurement in 0.1 M $HClO_4$ at 25 ^oC on a gold electrode. CO stripping was performed on the catalyst to obtain an $ECSA_{Ir}$ of 125 $m^2\ g^{-1}$, which was much higher than that found in prior work on iridium electrocatalysts. Oxidation of metallic iridium to iridium oxide was performed by cyclic voltammetry in the voltage range of 0.05-1.6 V_{RHE}. Hydrogen adsorption/desorption region was observed to disappear confirming the transformation to iridium oxide. The initial mass normalized OER activity of the catalyst was measured by chronoamperometry to be 75 A g_{Ir}^{-1}, which was six times higher than the standard IrO_2-AA. A Tafel plot for the catalyst was constructed from the CA data to yield a Tafel slope of 43 mV dec^{-1}. The RDS associated with this Tafel slope value has two proposed mechanistic pathways, the electrochemical oxide path or the DFT-predicted peroxide path. The specific activity of the catalyst was calculated to be 6.8 x 10^{-5} A cm^{-2}. While the tested catalyst did perform better than an iridium oxide standard material, the stability could be improved. Further studies are needed to i) understand the degradation mechanism for TiO_2-N800-Ir-EO; ii) further probe the degree of interaction between the active catalyst and support material; and iii) determine the effect of size on the catalytic activity of iridium deposited on an oxynitride support material. Increased temperature or dwell time of TiO_2 nanosheets could affect the degree of nitridation, which could further improve the conductivity of the material and promote enhanced interaction between the support and deposited catalyst.

LITERATURE CITED

1. Chao, J. Reimagining Hydrogen: A Small Molecule With Large-Scale Ideas. (accessed October).
2. Ramachandran, R.; Menon, R. K., An overview of industrial uses of hydrogen. *International Journal of Hydrogen Energy* **1998,** *23* (7), 593-598.
3. Sharma, S.; Ghoshal, S. K., Hydrogen the future transportation fuel: from production to applications. *Renewable and sustainable energy reviews* **2015,** *43*, 1151-1158.
4. Steinke, F.; Wolfrum, P.; Hoffmann, C., Grid vs. storage in a 100% renewable Europe. *Renewable Energy* **2013,** *50*, 826-832.
5. Abbasi, T.; Abbasi, S., 'Renewable'hydrogen: prospects and challenges. *Renewable and Sustainable Energy Reviews* **2011,** *15* (6), 3034-3040.
6. Hassan, S. Z.; Mumtaz, S.; Kamal, T.; Khan, L. In *Performance of grid-integrated photovoltaic/fuel cell/electrolyzer/battery hybrid power system*, Power Generation System and Renewable Energy Technologies (PGSRET), 2015, IEEE: 2015; pp 1-8.
7. Bockris, J. O. M., Kinetics of activation controlled consecutive electrochemical reactions: anodic evolution of oxygen. *The Journal of Chemical Physics* **1956,** *24* (4), 817-827.
8. Spöri, C.; Kwan, J. T. H.; Bonakdarpour, A.; Wilkinson, D. P.; Strasser, P., The stability challenges of oxygen evolving catalysts: towards a common fundamental understanding and mitigation of catalyst degradation. *Angewandte Chemie International Edition* **2017,** *56* (22), 5994-6021.
9. Energy.gov Hydrogen Production Pathways. https://www.energy.gov/eere/fuelcells/hydrogen-production-pathways.

10. Reier, T.; Nong, H. N.; Teschner, D.; Schlögl, R.; Strasser, P., Electrocatalytic oxygen evolution reaction in acidic environments–reaction mechanisms and catalysts. *Advanced Energy Materials* **2017,** *7* (1).

11. Park, S.; Shao, Y.; Liu, J.; Wang, Y., Oxygen electrocatalysts for water electrolyzers and reversible fuel cells: status and perspective. *Energy & Environmental Science* **2012,** *5* (11), 9331-9344.

12. Miles, D. T., Run-DMC: A Mnemonic Aid for Explaining Mass Transfer in Electrochemical Systems. *Journal of Chemical Education* **2013,** *90* (12), 1649-1653.

13. Cherevko, S.; Zeradjanin, A. R.; Topalov, A. A.; Kulyk, N.; Katsounaros, I.; Mayrhofer, K. J., Dissolution of noble metals during oxygen evolution in acidic media. *ChemCatChem* **2014,** *6* (8), 2219-2223.

14. Carmo, M.; Fritz, D. L.; Mergel, J.; Stolten, D., A comprehensive review on PEM water electrolysis. *International journal of hydrogen energy* **2013,** *38* (12), 4901-4934.

15. Millet, P.; Ngameni, R.; Grigoriev, S.; Fateev, V., Scientific and engineering issues related to PEM technology: Water electrolysers, fuel cells and unitized regenerative systems. *International Journal of Hydrogen Energy* **2011,** *36* (6), 4156-4163.

16. Reier, T.; Oezaslan, M.; Strasser, P., Electrocatalytic oxygen evolution reaction (OER) on Ru, Ir, and Pt catalysts: a comparative study of nanoparticles and bulk materials. *Acs Catalysis* **2012,** *2* (8), 1765-1772.

17. Cherevko, S.; Reier, T.; Zeradjanin, A. R.; Pawolek, Z.; Strasser, P.; Mayrhofer, K. J., Stability of nanostructured iridium oxide electrocatalysts during oxygen evolution reaction in acidic environment. *Electrochemistry Communications* **2014,** *48*, 81-85.

18. Wang, C.; Sui, Y.; Xu, M.; Liu, C.; Xiao, G.; Zou, B., Synthesis of Ni–Ir Nanocages with Improved Electrocatalytic Performance for the Oxygen Evolution Reaction. *ACS Sustainable Chemistry & Engineering* **2017,** *5* (11), 9787-9792.

19. Wu, Z.; Zou, Z.; Huang, J.; Gao, F., Fe-doped NiO mesoporous nanosheets array for highly efficient overall water splitting. *Journal of Catalysis* **2018,** *358*, 243-252.

20. Rodríguez-García, B.; Reyes-Carmona, Á.; Jiménez-Morales, I.; Blasco-Ahicart, M.; Cavaliere, S.; Dupont, M.; Jones, D.; Rozière, J.; Galán-Mascarós, J. R.; Jaouen, F., Cobalt hexacyanoferrate supported on Sb-doped SnO 2 as a non-noble catalyst for oxygen evolution in acidic medium. *Sustainable Energy & Fuels* **2018**.

21. Hao, C.; Lv, H.; Mi, C.; Song, Y.; Ma, J., Investigation of Mesoporous Niobium-Doped TiO2 as an Oxygen Evolution Catalyst Support in an SPE Water Electrolyzer. *ACS Sustainable Chemistry & Engineering* **2015,** *4* (3), 746-756.

22. Oh, H.-S.; Nong, H. N.; Reier, T.; Bergmann, A.; Gliech, M.; Ferreira de Araújo, J.; Willinger, E.; Schlögl, R.; Teschner, D.; Strasser, P., Electrochemical catalyst–support effects and their stabilizing role for IrO x nanoparticle catalysts during the oxygen evolution reaction. *Journal of the American Chemical Society* **2016,** *138* (38), 12552-12563.

23. Kumar, A.; Ramani, V., Strong metal–support interactions enhance the activity and durability of platinum supported on tantalum-modified titanium dioxide electrocatalysts. *Acs Catalysis* **2014,** *4* (5), 1516-1525.

24. Auer, G.; Woditsch, P.; Westerhaus, A.; Kischkewitz, J.; Griebler, W. d.; Rohe, M.; Liedekerke, M., Pigments, inorganic, 2. White pigments. *Ullmann's Encyclopedia of Industrial Chemistry* **2012**.

25. Jia, J.; Yamamoto, H.; Okajima, T.; Shigesato, Y., On the Crystal Structural Control of Sputtered TiO2 Thin Films. *Nanoscale research letters* **2016,** *11* (1), 324.

26. Chu, L.; Qin, Z.; Yang, J., Anatase TiO 2 nanoparticles with exposed {001} facets for efficient dye-sensitized solar cells. *Scientific reports* **2015,** *5*, 12143.

27. Bewer, G.; Debrodt, H.; Herbst, H., Titanium for electrochemical processes. *JOM* **1982,** *34* (1), 37-41.

28. Cao, X.; Tian, G.; Chen, Y.; Zhou, J.; Zhou, W.; Tian, C.; Fu, H., Hierarchical composites of TiO 2 nanowire arrays on reduced graphene oxide nanosheets with enhanced photocatalytic hydrogen evolution performance. *Journal of Materials Chemistry A* **2014,** *2* (12), 4366-4374.

29. Liu, S.; Jia, H.; Han, L.; Wang, J.; Gao, P.; Xu, D.; Yang, J.; Che, S., Nanosheet-constructed porous TiO2–B for advanced lithium ion batteries. *Advanced Materials* **2012,** *24* (24), 3201-3204.

30. Lusvardi, G.; Barani, C.; Giubertoni, F.; Paganelli, G., Synthesis and Characterization of TiO2 Nanoparticles for the Reduction of Water Pollutants. *Materials* **2017,** *10* (10), 1208.

31. Mazúr, P.; Polonský, J.; Paidar, M.; Bouzek, K., Non-conductive TiO2 as the anode catalyst support for PEM water electrolysis. *international journal of hydrogen energy* **2012,** *37* (17), 12081-12088.

32. Oakton, E.; Lebedev, D.; Povia, M.; Abbott, D. F.; Fabbri, E.; Fedorov, A.; Nachtegaal, M.; Copéret, C.; Schmidt, T. J., IrO2-TiO2: A High-Surface-Area, Active, and Stable Electrocatalyst for the Oxygen Evolution Reaction. *ACS Catalysis* **2017,** *7* (4), 2346-2352.

33. Moradi, F.; Dehghanian, C., Addition of IrO2 to RuO2+ TiO2 coated anodes and its effect on electrochemical performance of anodes in acid media. *Progress in Natural Science: Materials International* **2014,** *24* (2), 134-141.

34. Fuentes, R. E.; Farell, J.; Weidner, J. W., Multimetallic electrocatalysts of Pt, Ru, and Ir supported on anatase and rutile TiO2 for oxygen evolution in an acid environment. *Electrochemical and Solid-State Letters* **2011,** *14* (3), E5-E7.

35. Shin, H.; Kim, H.-i.; Chung, D. Y.; Yoo, J. M.; Weon, S.; Choi, W.; Sung, Y.-E., Scaffold-like titanium nitride nanotubes with a highly conductive porous architecture as a nanoparticle catalyst support for oxygen reduction. *Acs Catalysis* **2016,** *6* (6), 3914-3920.

36. Kakinuma, K.; Wakasugi, Y.; Uchida, M.; Kamino, T.; Uchida, H.; Deki, S.; Watanabe, M., Preparation of titanium nitride-supported platinum catalysts with well controlled morphology and their properties relevant to polymer electrolyte fuel cells. *Electrochimica Acta* **2012,** *77*, 279-284.

37. Avasarala, B.; Murray, T.; Li, W.; Haldar, P., Titanium nitride nanoparticles based electrocatalysts for proton exchange membrane fuel cells. *Journal of Materials Chemistry* **2009,** *19* (13), 1803-1805.

38. Gebauer, C.; Fischer, P.; Wassner, M.; Diemant, T.; Jusys, Z.; Hüsing, N.; Behm, R., Performance of titanium oxynitrides in the electrocatalytic oxygen evolution reaction. *Nano Energy* **2016,** *29*, 136-148.

39. Alia, S. M.; Rasimick, B.; Ngo, C.; Neyerlin, K.; Kocha, S. S.; Pylypenko, S.; Xu, H.; Pivovar, B. S., Activity and Durability of Iridium Nanoparticles in the Oxygen Evolution Reaction. *Journal of The Electrochemical Society* **2016,** *163* (11), F3105-F3112.

40. Zhang, Z.; Chu, Q.; Li, H.; Hao, J.; Yang, W.; Lu, B.; Ke, X.; Li, J.; Tang, J., One-pot solvothermal synthesis of graphene-supported TiO2 (B) nanosheets with enhanced lithium storage properties. *Journal of colloid and interface science* **2013,** *409*, 38-42.

41. Livage, J.; Henry, M.; Sanchez, C., Sol-gel chemistry of transition metal oxides. *Progress in solid state chemistry* **1988,** *18* (4), 259-341.

42. Cushing, B. L.; Kolesnichenko, V. L.; O'Connor, C. J., Recent advances in the liquid-phase syntheses of inorganic nanoparticles. *Chemical reviews* **2004,** *104* (9), 3893-3946.

43. Li, J.; Gao, L.; Sun, J.; Zhang, Q.; Guo, J.; Yan, D., Synthesis of nanocrystalline titanium nitride powders by direct nitridation of titanium oxide. *Journal of the American Ceramic Society* **2001,** *84* (12), 3045-3047.

44. Ding, Z.; Cheng, Q.; Zou, L.; Fang, J.; Zou, Z.; Yang, H., Controllable synthesis of titanium nitride nanotubes by coaxial electrospinning and their application as a durable support for oxygen reduction reaction electrocatalysts. *Chemical Communications* **2017,** *53* (99), 13233-13236.

45. Chen, T.-T.; Liu, H.-P.; Wei, Y.-J.; Chang, I.-C.; Yang, M.-H.; Lin, Y.-S.; Chan, K.-L.; Chiu, H.-T.; Lee, C.-Y., Porous titanium oxynitride sheets as electrochemical electrodes for energy storage. *Nanoscale* **2014,** *6* (10), 5106-5109.

46. Uen, W.-Y.; Li, Z.-Y.; Lan, S.-M.; Yang, T.-N.; Liao, S.-M., Fabrication of low-resistivity and gold-colored TiN films by halide chemical vapor deposition with a low [NH3]/[TiCl4] flow ratio. *Thin Solid Films* **2007,** *516* (1), 99-103.

47. Chen, H.; Nambu, A.; Wen, W.; Graciani, J.; Zhong, Z.; Hanson, J. C.; Fujita, E.; Rodriguez, J. A., Reaction of NH3 with titania: N-doping of the oxide and TiN formation. *The Journal of Physical Chemistry C* **2007,** *111* (3), 1366-1372.

48. Anbukarasu, P. *Pulsed Laser Deposition of Epitaxial Titanium Nitride on Magnesium Oxide substrate*; Graduate School of Science, University of Tokyo: 2012.

49. Williams, D.; Baiocchi, F.; Beairsto, R.; Brown, J.; Knoell, R.; Murarka, S., Nitrogen, oxygen, and argon incorporation during reactive sputter deposition of titanium nitride. *Journal of Vacuum Science & Technology B: Microelectronics Processing and Phenomena* **1987,** *5* (6), 1723-1729.

50. Sun, Y.; Xia, Y., Shape-controlled synthesis of gold and silver nanoparticles. *Science* **2002,** *298* (5601), 2176-2179.

51. Hei, H.; He, H.; Wang, R.; Liu, X.; Zhang, G., Controlled synthesis and characterization of noble metal nanoparticles. *Soft Nanoscience Letters* **2012,** *2* (03), 34-40.

52. Nguyen, T. D.; Scherer, G. G.; Xu, Z. J., A facile synthesis of size-controllable IrO2 and RuO2 nanoparticles for the oxygen evolution reaction. *Electrocatalysis* **2016,** *7* (5), 420-427.

53. Spenadel, L.; Boudart, M., Dispersion of platinum on supported catalysts. *The Journal of Physical Chemistry* **1960,** *64* (2), 204-207.

54. Offer, G.; Kucernak, A., Calculating the coverage of saturated and sub-saturated layers of carbon monoxide adsorbed onto platinum. *Journal of Electroanalytical Chemistry* **2008,** *613* (2), 171-185.

55. Grgur, B. N.; Markovic, N. M.; Lucas, C. A.; ROSS, P. N., Electrochemical oxidation of carbon monoxide: from platinum single crystals to low temperature fuel cells catalysts. Part I: Carbon monoxide oxidation onto low index platinum single crystals. *Journal of the Serbian Chemical Society* **2001,** *66* (11-12), 785-797.

56. Alia, S. M.; Hurst, K. E.; Kocha, S. S.; Pivovar, B. S., Mercury Underpotential Deposition to Determine Iridium and Iridium Oxide Electrochemical Surface Areas. *Journal of The Electrochemical Society* **2016,** *163* (11), F3051-F3056.

57. Zhao, S.; Yu, H.; Maric, R.; Danilovic, N.; Capuano, C. B.; Ayers, K. E.; Mustain, W. E., Calculating the electrochemically active surface area of iridium oxide in operating proton exchange membrane electrolyzers. *Journal of The Electrochemical Society* **2015,** *162* (12), F1292-F1298.

58. Juodkazytė, J.; Šebeka, B.; Valsiunas, I.; Juodkazis, K., Iridium anodic oxidation to Ir (III) and Ir (IV) hydrous oxides. *Electroanalysis* **2005,** *17* (11), 947-952.

59. Godínez-Salomón, F. A., L.; Alia, S.; Pivovar, B.; Camacho-Forero, L.; Balbuena, P; Mendoza-Cruz, R.; Arellano-Jimenez, M.J.; Rhodes, C.P Self-Supported Hydrous Iridium-Nickel Oxide Two-dimensional Nanoframes for High Activity Oxygen Evolution Electrocatalysts. 2018.

60. Doyle, R. L.; Lyons, M. E., The oxygen evolution reaction: mechanistic concepts and catalyst design. In *Photoelectrochemical solar fuel production*, Springer: 2016; pp 41-104.

61. Guidelli, R.; Compton, R. G.; Feliu, J. M.; Gileadi, E.; Lipkowski, J.; Schmickler, W.; Trasatti, S., Defining the transfer coefficient in electrochemistry: An assessment (IUPAC Technical Report). *Pure and Applied Chemistry* **2014,** *86* (2), 245-258.

62. Antolini, E., Iridium as catalyst and cocatalyst for oxygen evolution/reduction in acidic polymer electrolyte membrane electrolyzers and fuel cells. *ACS Catalysis* **2014,** *4* (5), 1426-1440.

63. Alia, S. M.; Shulda, S.; Ngo, C.; Pylypenko, S.; Pivovar, B. S., Iridium-based Nanowires as Highly Active, Oxygen Evolution Reaction Electrocatalysts. *ACS Catalysis* **2018**.

64. Lu, Z.-X.; Shi, Y.; Yan, C.-F.; Guo, C.-Q.; Wang, Z.-D., Investigation on IrO2 supported on hydrogenated TiO2 nanotube array as OER electro-catalyst for water electrolysis. *International Journal of Hydrogen Energy* **2017,** *42* (6), 3572-3578.

65. Nong, H. N.; Oh, H. S.; Reier, T.; Willinger, E.; Willinger, M. G.; Petkov, V.; Teschner, D.; Strasser, P., Oxide-Supported IrNiOx Core–Shell Particles as Efficient, Cost-Effective, and Stable Catalysts for Electrochemical Water Splitting. *Angewandte Chemie International Edition* **2015,** *54* (10), 2975-2979.